University of Leoben

Low Temperature Oxidation of Sputtered Thin Films of Molybdenum Alloys

Diploma Thesis

by

Andrea List

Leoben, June 2009

This work has been carried out in cooperation with PLANSEE Metall GmbH Reutte, Austria, Department of General, Analytical and Physical Chemistry, University of Leoben, Austria and Department of Physical Metallurgy and Materials Testing, University of Leoben, Austria.

Affidavit

I declare in lieu of oath, that I wrote this thesis and performed the associated research myself, using only literature cited in this volume.

Leoben, June 2009

_____

(Andrea List)

Acknowledgements

This work has been carried out in cooperation with PLANSEE Metall GmbH Reutte, Austria, Department of General, Analytical and Physical Chemistry, University of Leoben, Austria and Department of Physical Metallurgy and Materials Testing, University of Leoben, Austria.

My sincerest gratitude and appreciation are due to my supervisor ao.Univ.Prof. DI. Dr. Christian Mitterer, Head of the Thin Film Group at the Department of Physical Metallurgy and Materials Testing and my co-supervisor ao. Univ. Prof, DI. Dr. Gregor Mori, Department of General, Analytical and Physical Chemistry, for their help and guidance and giving an expertise to this thesis.

My deepest appreciation to Dr. Jörg Winkler, Dr. Nikolaus Reinfried and Dr. Wolfram Knabl PLANSSE GmbH, Austria, for their perfect support during the thesis.

Sincere thanks to all my colleagues at the Department of Physical Metallurgy and Materials Testing and especially the Thin Film People and my colleagues at the Department of General, Analytical and Physical Chemistry for their great support I received in all matters.

My final thanks to my family and friends, for their love, friendship and support. Without them, everything would have been far more difficult. Special thanks to my sister Martina for her friendship and encouragement.

Contents

1. Introduction

Sputtered Molybdenum (Mo) thin films are widely used for thin-film-transistor (TFT) data lines due their relatively low electrical resistance and easy chemical patterning. They are often used as a single data line or as a capping layer on top of aluminium. Thin-film deposition by sputtering is a key process step in the manufacture of TFT materials that are successively deposited and patterned. Mo has a straight-line expansion and is suitable for sealing to hard glass since it has approximately the same coefficient of expansion and a transition temperature below 700°C [1, 2]. TFTs are similar to transistors used in semiconductor chips. In terms of switching speed and operating voltage, they are inferior to state of the art MOS transistors in crystalline silicium. However, they are quite adequate as a simple ON/OFF pixel switch with a 60 Hz refresh rate. TFTs can be used in combination with several display effects (LCD, OLED, ELD, E-Ink, ECD); each pixel is driven by one TFT. TFTs consist of thin films of metals, semiconductor- and insulator materials [3]. Fig. 1.1 shows a sectional view of a TFT with a Mo full capped Al (Mo/Al) film [4].

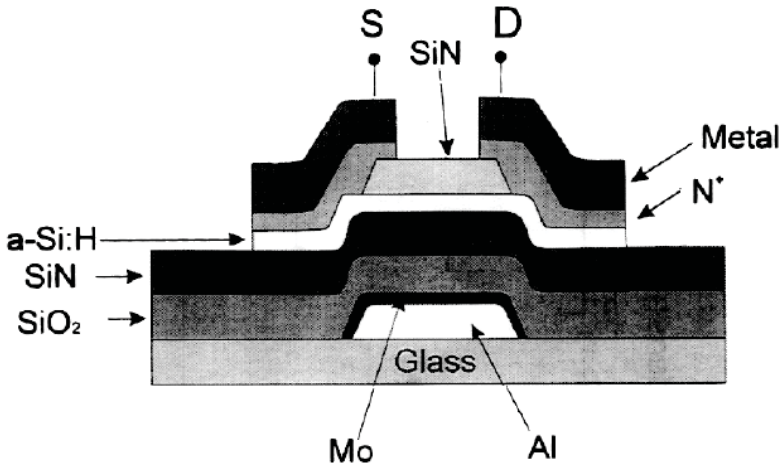

Figure 1.1: The cross sectional view of a-Si:H TFT fabricated by using a Mo/Al gate film [4].

Corrosion of Mo in the production process of TFT causes serious problems and their storage in moist air leads to superficial oxidation of Mo. Although, the oxidation behaviour at high temperatures has been investigated intensively, little is known about corrosion behaviour of Mo thin films at room temperature [6, 7]. The increasing demand for sputtered Mo thin films in TFT industry defy the fundamental electrochemical study on the film. The lack of a systematic study of the effect of low contents of alloying elements in

sputter deposited Mo films on their oxidation behaviour and corrosion resistance was the main driving force for the present investigation. The aim of this work is to synthesize Mo thin films alloyed with low contents of Ti, Cr, Ni, Nb, Ta or W, respectively on glass substrates by magnetron sputter deposition from mosaic targets and to examine the corrosion behaviour of these alloys during exposure in a climatic test chamber and by different electrochemical measurements in 0.9 % NaCl aqueous solution.

2. Physical Vapour Deposition

2.1. General

Physical Vapour Deposition (PVD) is the most suitable technique to deposit thin films with practically no limitation on chemical composition. Up to now many process variations and modifications have been developed and are in industrial use [8, 9,10].

Reduced to its essence, PVD involves three steps [8, 9]:

1. Generation of the vapours by thermal energy (evaporation) or by momentum transfer (sputtering).
2. Transport of the vaporized material through the pressure-reduced atmosphere from the source to a substrate. During their transport collisions with residual gas molecules depending on vacuum conditions and source to substrate distance can occur.
3. Condensation at the substrate and finally formation of a deposit by heterogeneous nucleation and film growth.

There is a common classification based on the different basic types of film deposition techniques. These are coating by evaporation, sputtering, and ion plating.
Evaporation and sputtering are basic PVD processes (see Fig. 2.1), whereas Ion Plating is a further development of these main methods [8, 10].
Following, a brief introduction of these three methods is given.

In the **evaporation deposition** process a heat source is utilized to vaporize material (Fig. 1a). Resistance, induction, arc, electron beam or lasers are typical heat sources. Evaporation is usually carried out under a low pressure atmosphere 10^{-8} to 10^{-3} Pa, maximizing the mean free path to support a line-of-sight flight of vaporised atoms/ions, or at least causing only a few collisions. High evaporation rate can be reached and the coatings are suitable for uniform coverage of planar substrates [9, 11].
Sputtering is a vaporization process where the source material (target) is subjected to ion bombardment of sufficiently high energy, resulting in the direct ejection of surface atoms

from the solid into the vapour state (Fig. 1b). To generate the ion bombardment, a high voltage source and an inert working gas is needed. A glow discharge plasma is ignited between the target and the substrate. Sputter deposition processes are well suited to deposit refractory metals, alloys and compounds. In this work a sputtering system has been used. Therefore this process will be described more precisely later on [8, 12, 13].

Ion plating is a process that uses thermal energy or momentum transfer for vaporizing the coating material (Fig. 1c).The main difference to evaporation and sputtering is that some of the vaporized atoms are ionized by a glow discharge. The coating material is accelerated within the electric field to the substrate by an applied negative substrate bias voltage [8, 13].

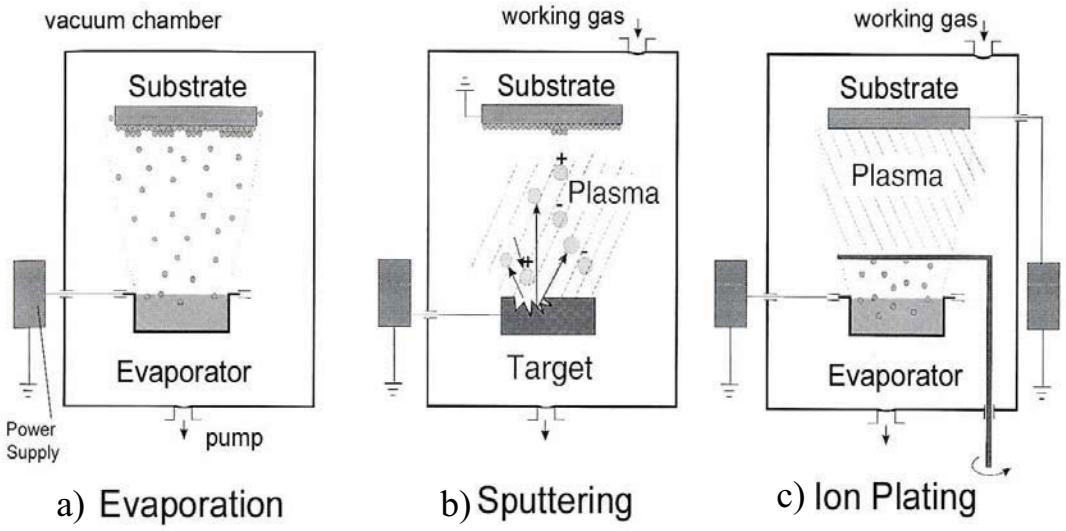

Figure 2.1: PVC basic processes [modified after 13], a) evaporation, b) sputtering, c) ion plating

2.1.1. Plasma / Gas discharge

Usually, ion plating and sputtering take place in the presence of a plasma environment, so called fourth state of matter. A plasma is a mixture of gas atoms (e.g. argon) or molecules (e.g. nitrogen), positive charged ions and negative charged electrons moving in random directions. The number of positive and negative particles is equal and therefore the plasma is in average electrical neutral (quasineutral). By the movement of the charged particles electrical fields are generated.

In low pressure processing discharges, as used in PVD processes, an applied electrical power mainly influences the electrons. They are accelerated, gain energy and their temperature increases up to 10^5 K. The heavier ions are less affected and their temperature remains almost at room temperature, but they transfer their energy by collision with the background gas. On account of the differing temperatures of the electrons and the heavy ions, a thermodynamic equilibrium cannot be reached. The temperature stays relatively low because the electron temperature contributes only a few to the overall temperature. Therefore, such a plasma is called cold plasma [13, 14]. A gas discharge is a phenomenon where electrical charges are transported in a gas or vapor by mobile charge carriers (ions, electrons). The different steps of forming a direct current (DC) gas discharge can be discussed based on the current/voltage (see Fig 2.2). By applying a voltage between two electrodes, first a very small current flow is affected in the gas because only a small amount of ionized particles exist which can contribute to the current. With increasing voltage, the charged particles gain sufficient energy in order to produce additional charged particles by impact ionization. This leads to a linear growth of the discharge current, where the voltage stays constant. This range is called Townsend discharge. Ions strike on the negative charged cathode and release secondary electrons. These are accelerated in the electric field and due collisions with the residual gas atoms new ions are generated, which are again accelerated to the cathode and produce new secondary electrons. If the amount of generated electrons is sufficient to produce so many ions that can again produce the same number of electrons the discharge is self-maintaining.

Upon further increase of power the discharge begins to glow. This range is called normal discharge, the voltage falls and the current rises abruptly. The current is now proportional to the electrode area covered by the glow discharge. When the glow discharge covers the whole electrode area, increasing of the applied power causes a rise of current and voltage. This area corresponds to the abnormal discharge, and is used for cathode sputtering.

A further increase in current changes the glow discharge into an arc discharge. The cathode now collects a big number of positive ions with higher energy than before, and thus the cathode temperature goes up. This leads to thermionic emission. Because of the high current and high ionization rate, this behavior is used in arc based deposition processes [13, 7, 8].

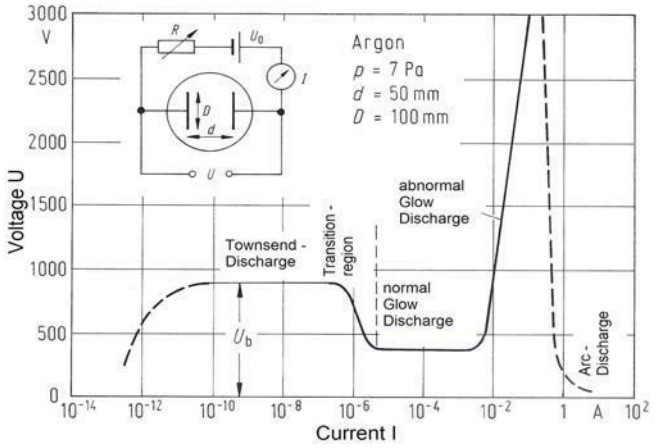

Figure 2.2: Current-voltage characteristics of a gas discharge process [9].

2.2. Sputtering

As briefly mentioned in section 2.1, sputtering is the effect of direct ejection of surface atoms by momentum transfer from bombarding with noble gas ions, usually Ar^+ ions. The ions are provided by the working gas in a glow discharge.

The process takes place in a vacuum chamber, which has been evacuated to low pressures. A sputtering system consists of a cathode (target) and an anode. The positive ions produced in the gas discharge are accelerated to the negative target. Upon bombardment, they cause ejection of mainly neutral particles by impulse transfer. The ejected particles move through the working gas and condense on the substrate as well as on the chamber walls. Figure 2.3 shows the particle interactions which can occur during the sputter process [9, 15].

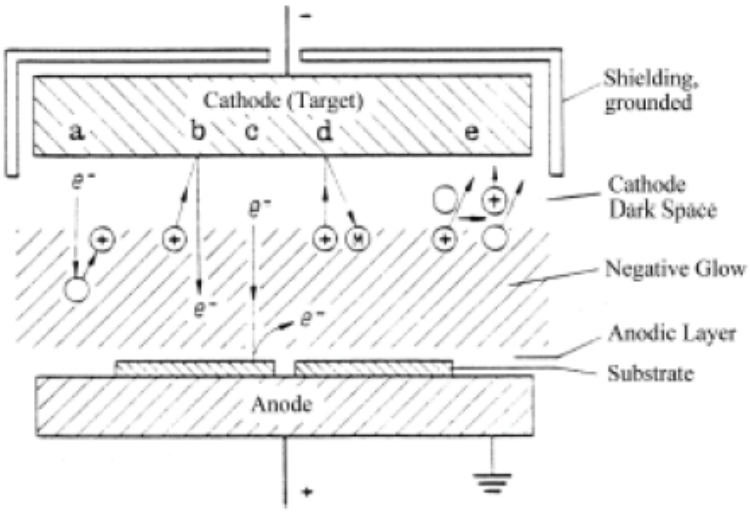

Figure 2.3: Possible particle interactions during sputtering: (a) Ionisation by electron impact, (b) Ion induced electron emission from cathode, (c) Electron induced emission of secondary electrons from anode, (d) Sputtering caused by ion impact, (e) Charge transition process [9].

Sputtering of a target by energetic ions is assumed to result from cascades of atomic collisions. The average number of atoms ejected from the target per incident ion is called sputter yield and depends on angle of incidence, mass ratio and surface energy. Furthermore, the condition of the target (roughness, crystalline structure, temperature) and the target material `s sublimations heat have an effect on the sputtering yield.
Sputter deposition systems can be powered by DC or by radio frequency (RF), which is mainly used for deposition of non-conducting materials [8].

2.2.1. Diode Sputtering

Diode sputtering represents the simplest sputter arrangement. Two electrodes facing each other are installed in a vacuum chamber. One of them, the target, is at high negative potential which maintains the glow discharge by producing secondary electrons. Furthermore, the target serves as material source for the films to be produced. The substrates are placed opposite the target, which can be grounded or applied to negative potential (bias voltage). Such a system usually needs water cooling from the target backside, because due to the high ion currents accelerated to the target high temperatures are reached. The typical working gas pressure is approximately a few Pa. To establish a glow discharge a minimum gas pressure is necessary. At low pressure the mean free path of particles increases and the number of collisions decreases; as a result the mean energy of

ions increases. However, the effect of an increased energy of ions is not sufficient to compensate the effect of a decrease in ion density. A high ion density is required for reasonable deposition rates. Moreover, the ions are generated relatively far away from the target and thus they have a higher probability to loose energy on their way [8, 10, 16].

2.2.2. Magnetron Sputtering

One of the major disadvantages of the diode setup is its rather low coating growth yield. With a magnetron cathode, the plasma electrons are confined by an additional magnetic field and therefore the ionization efficiency close to the target can be significantly increased. The larger electron density causes higher ion currents und higher sputtering rates at lower working gas pressures. Because the magnetic field has only a strength of a few hundred Gauss, it influences only electrons but not ions [8, 15, 16]. The magnetic field concentrates the plasma near the cathode and forms a drifting, circulating current, the so called "racetrack" area. This leads to a non uniform erosion of the target surface (Fig. 2.4).

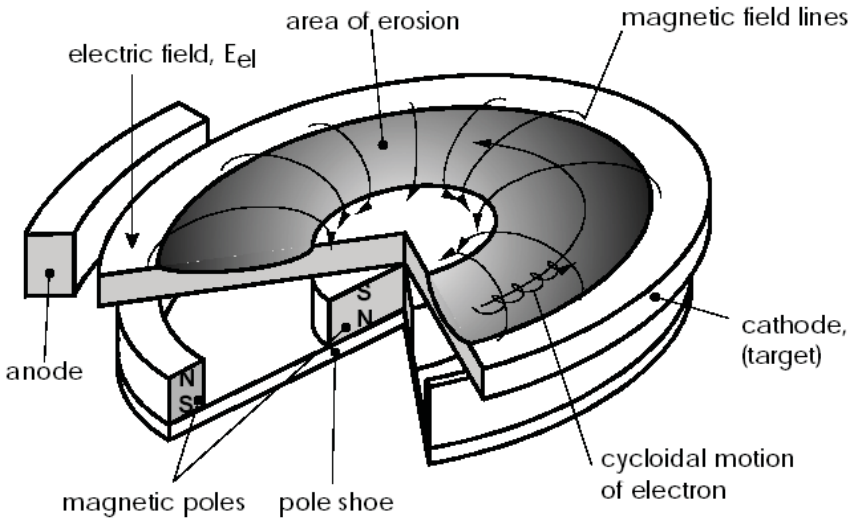

Figure 2.4: Planar magnetron configuration with racetrack area of erosion [15].

Two different magnetrons systems can be distinguished depending on the course of the magnetic fields: the conventional balanced magnetron (CBM) and the unbalanced magnetron (UBM). The conventional balanced magnetron configuration forces the discharge close to the target. All magnetic field lines form an ideal loop between the inner and outer magnets of the planar magnetron, which means that they are balanced against each other. In unbalanced magnetrons, some magnetic field lines do not loop, they are

open towards the substrates shown in Fig. 2.5. This is feasible by stronger inner or outer magnets of the magnetron setup [10, 11, 14].

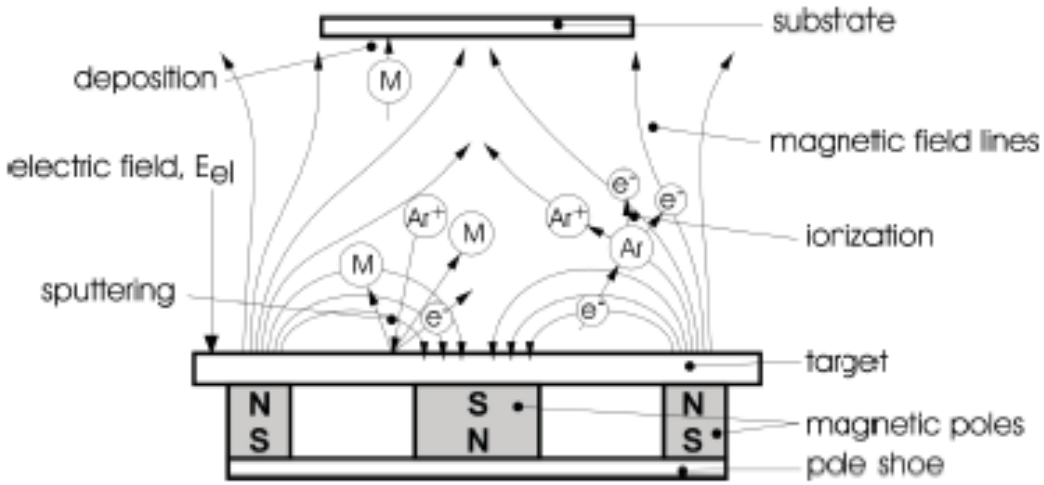

Figure 2.5: Schematic of an unbalanced magnetron configuration [17].

Therefore an expansion of the plasma away from the target surface is possible and enables an adjustment of the plasma density close to the substrate by varying the magnetic field or by applying a negative potential to the substrate (bias voltage). As a result, the growing film is also bombarded by energetic ions and consequently the microstructure of the growing film is effected positively, where the energy of the impinging ions can be regulated [8,18].

2.3. Morphology of thin films

2.3.1. Nucleation and growth

Nucleation and film growth determine the coating structure and the coating properties, which are normally different to their respective bulk materials. From the gas phase atoms are impinging on the substrate with a certain arrival rate, where they are adsorbed or directly reflected. In the case of adsorption, there are several reactions during the formation of atoms to clusters and nuclei, as shown in Fig. 2.6. The further enlargement of nuclei by arrival of deposition atoms is called growth.

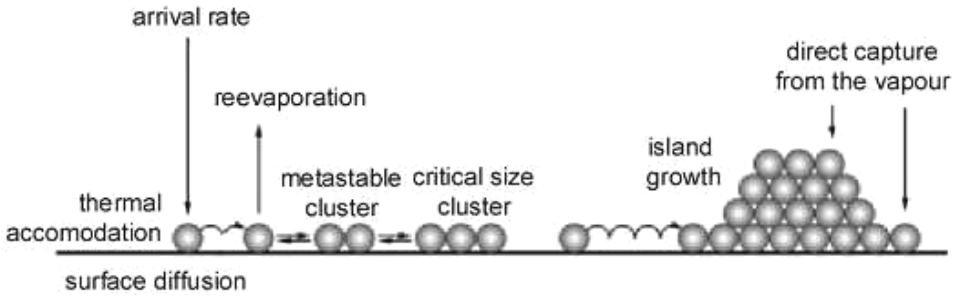

Figure 2.6: Schematic of nucleation and growth processes [17].

The nucleation and growth steps during the formation of a continuous film are usually as follows [19]:

- Condensation of absorbed ad-atoms
- Formation of subcritical and critical nuclei in the nucleation stage
- Growth of these nuclei to supercritical dimensions with the resulting depletion of ad-atoms in the capture zone around them
- Concurrent with the previous steps there will be nucleation of critical clusters in areas not depleted of ad-atoms
- Clusters touch and coalesce to form a new island occupying an area smaller than the sum of the original two, thus exposing fresh substrate surface
- Ad-atoms adsorb on the freshly exposed areas and secondary nucleation occurs
- Large islands grow together, leaving channels or holes of exposed substrate
- The channels or holes fill via secondary nucleation to give a continuous film

As mentioned above, normally the substrate and the deposited coating have different chemical compositions. Hence, the vapour atoms will not immediately react with the surface but become loosely bonded forming the so called ad-atoms. The ad-atoms are able to diffuse or exchange their energy with other atoms or the lattice before the get desorbed again or become trapped at low energy lattice sites. Nucleation rate and growth of nuclei depend on impingement rate and the substrate temperature, the latter defining the surface diffusion and re-evaporation. Depending on the affinity of film and substrate, the activation energies between film-film and film-substrate, Fig. 2.7 shows three possible modes of crystal growth on substrates in the early stages.

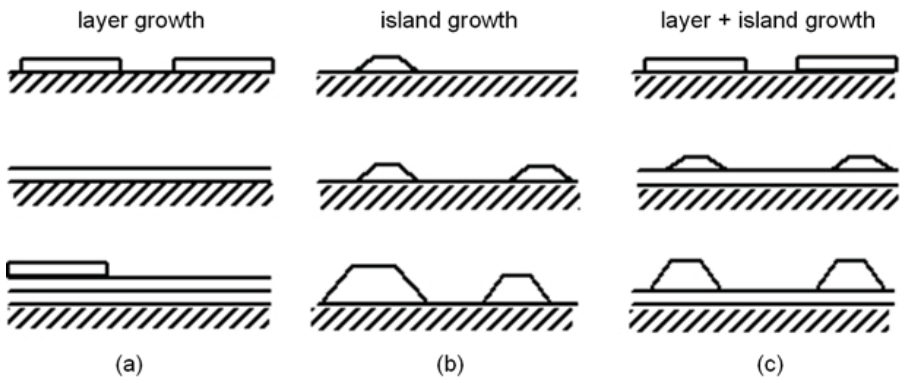

Figure 2.7: Schematic of three modes of film growth mechanisms. (a) Frank-van der Merwe, (b) Volmer-Weber, (c) Stranski-Krastanov model [20].

The layer growth or Frank-van der Merwe mode (Fig. 2.7a) is characterised by atoms which are more strongly bound to the substrate than to each other and therefore form a complete monolayer. The island or the Volmer-Weber mode (Fig. 2.7b) displays the opposite characteristics. Small clusters are nucleated directly on the substrate surface and grow into islands. This happens when atoms are more strongly bound to each other than to the substrate. The layer plus island growth, or Stranski-Krastanov mode (Fig. 2.7c), is an intermediate case. At first there is formation of monolayers followed by island growth onto them [19-21].

2.3.2. Structure Zone Models

The necessity to give a systematic description of the coating structure depending on the deposition conditions has been realised in well known structure zone models (SZM) [8, 22]. More than 30 years ago Movchan and Demchishin published their SZM based on a single macroscopic parameter, the homologous temperature (T_s/T_m) of the substrate. Here, T_s is the substrate temperature and T_m is the melting temperature of the coating. They proposed three main structure zones. This simple model already reflects many experimental observations of thin film growth, since diffusion as the growth-determining factor is strongly related to T_s/T_m [23]. In order to extend these concept to differences in various deposition techniques, the influence of the sputtering gas pressure have been considered in the model of Thornton [24] (see Fig. 2.8 (a)). With increasing working gas pressure the kinetic energy of the impinging adatoms decreases due the rising number of collisions between the particles. Thornton also found a new zone, the transition zone T, between zone I and zone II. Thornton`s model was further modified by Messier et al [25] (see Fig. 2.8 (b)), considering the influence of the energy of the impinging ions, expressed

as a function of the bias voltage. Here, the T zone is extended in the lower temperature range, because ion bombardment induces mobility of the surface atoms.

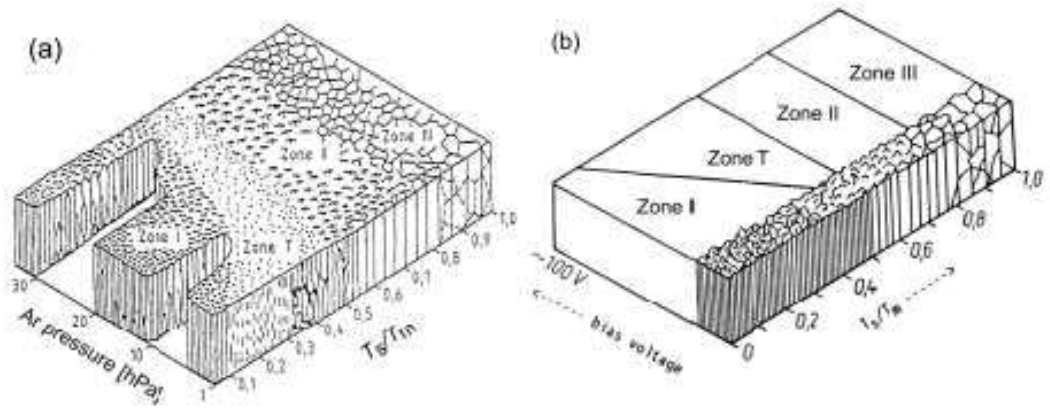

Figure 2.8 (a) Structure zone model (SZM) after Thornton [26] (b) modified SZM after Messier et al [24].

Generally, a reduction of the kinetic energy, whether by higher gas pressure or lower bias voltages, leads to a lower adatom mobility. Hence, higher deposition temperatures are necessary to determine a certain coating structure.

Zone 1 is characterized by fibrous, low dense grains and voided boundaries. The mobility of the adatoms is low, due the low substrate temperature (negligible surface diffusion). Higher argon pressure extends zone 1, while increasing T_s/T_m leads to larger crystals.

Zone T is the transition zone from Zone 1 to Zone 2. The homologous temperature ratio is higher, and thus the adatom mobility rises. This leads to a dense columnar structure with fibrous grains but no voids between the boundaries.

In Zone 2, surface diffusion controls the growth of the crystals, and the structure consists of coarser columnar grains with tight grain boundaries. The column diameter increases with higher homologous temperature ratio.

Zone 3 exhibits large equiaxed grains (recrystallized grain structure) and a smooth surface is formed. Bulk diffusion is assumed to be the dominating process [9, 25-28].

Fig. 2.9 shows that under various conditions, different SZM`s of vapour deposited coatings develop. Generally, deposited coatings grow from initial nuclei in the direction of available coating flux, only those nuclei with favourable growth properties and deposition conditions survive. In case of zero surface diffusion and a unity condensation coefficient, Fig. 2.9(a), a dense columnar coating structure with a relatively smooth surface topography is formed. If no crystal surface discrimination exists, the initial nuclei are spherical. Affected by a slightly varying direction of impinging atoms, the structure is grown in zone T shape.

Fig. 2.9 (b) illustrates the case if the initial nuclei have different orientations, and therefore different surface energies and sticking coefficients exist. Hence, the low energy faces grow faster; as a result the coating structure is open with relatively rough surface, corresponding to Zone 1. Fig. 2.9 (c) shows a dense columnar structure with a smooth but facetted surface. In case of higher T_s, the dependence on the condensation coefficient can be compensated. All crystals grow with the same rate (Zone 2). Infinite surface diffusion and periodic nucleation on the surface of growing crystals may lead to a structure shown in Fig. 2.9 (d)

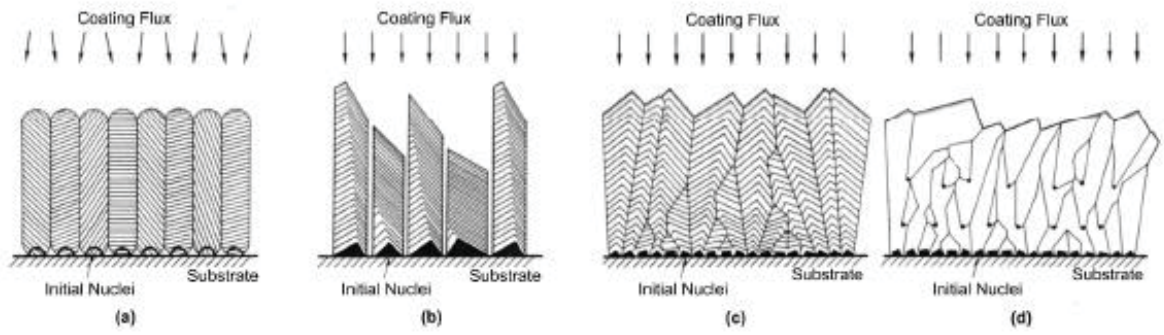

Figure 2.9: Structure development for several cases of adatom surface diffusion. (a) Zero surface diffusion, equal condensation coefficient. (b) Zero surface diffusion, dependence of condensation coefficient on crystallographic surface. (c) Infinite surface diffusion. (d) Infinite surface diffusion with periodic nucleation [29].

The morphological influence of impurities changes Thorntons`s SZM, therefore, other "real" SZM`s have been developed, illustrated in Fig. 2.10. However, not only contamination by foreign species like vapour or oxygen but also deliberately deposited alloying elements can be considered as impurities. Usually, the foreign particles cause decreasing surface mobility and low diffusion processes. Increasing content of impurity leads to a change of the zone transition temperatures as well as grain refinement [26, 27].

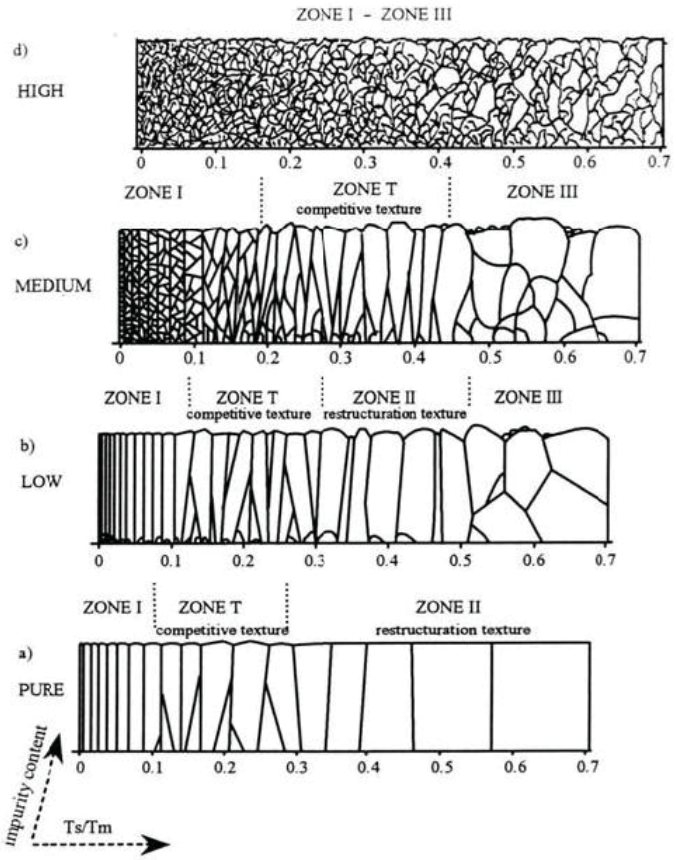

Figure 2.10: Ideal (a), and real SZM with increasing impurity content: low (b), medium (c) and high (d) [27].

3. Corrosion

3.1. General

Corrosion is a major economical problem. In most industrial countries annual corrosion cost are as high as 4 % of gross national product. Therefore it is an important aim of high-technology industries to find methods to reduce corrosion. Generally speaking, corrosion may be defined as an attack on a material through reaction with a surrounding medium which results in material degradation or loss [5, 30].

3.2. Forms of corrosion

Corrosion can manifest itself in many forms such as: uniform corrosion, intergranular corrosion, pitting corrosion and stress corrosion [5, 30]. Fig. 3.1 shows schematically different types of corrosion [31].

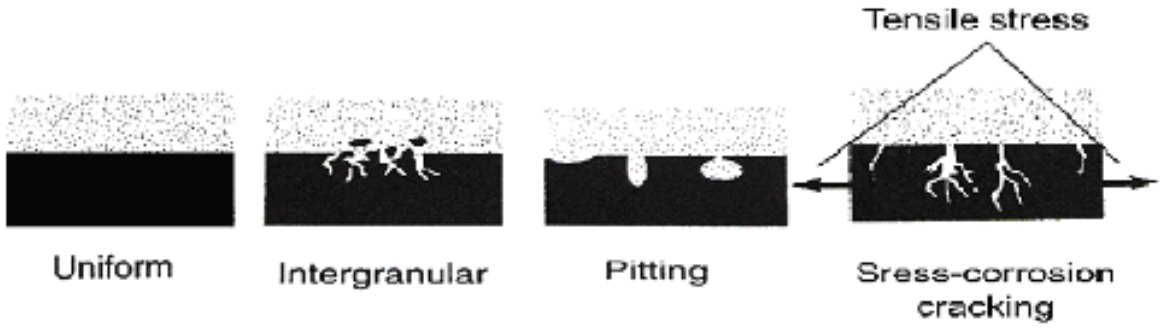

Figure 3.1 Types of corrosion [31].

The corrosion behaviour of thin films is strongly dependent on the structures of the film [32] and following corrosion phenomena considered:

The most common form of corrosion is the **uniform or general corrosion**. It is characterized by a chemical or electrochemical reaction which takes place uniformly over the exposed surface. The film becomes thinner and eventually results in perforation and failure [5].

Intergranular corrosion consists of localized attack at grain boundaries and results in disintegration of the metal. Since the grain boundary is composed of broken bonded atoms, the corrosion occurs preferentially on the grain-boundaries. Consequently, as the grain-boundary increased the susceptibility of corrosion becomes higher [5, 32].

Pitting corrosion causes localized penetration of the metal. When the protective oxide film of the metal is locally dissolved, usually by attack of aggressive anions such as chloride, the unprotected metal will be dissolved. A similar type of corrosion can take place, when the coating has flaws or micropores [5, 26].

3.3. Corrosion Phenomena

The present study deals with wet corrosion. Therefore a short overview about the chemical reactions working place during wet corrosion is given. When a metal is corroded by an electrolyte, an anodic and a cathodic reaction take place simultaneously. On the anodic site of the metal surface an oxidizing reaction occurs, such as (equation 3.1):

$$Me \rightarrow Me^{n+} + ne^- \qquad (3.1)$$

The free electrons migrate to cathodic sites where the can reach according to the following reduction reactions (equations 3.2 to 3.4):

$$O_2 + 4\,H^+ + 4\,e^- \rightarrow 2\,H_2O \qquad (3.2)$$

$$O_2 + 2\,H_2O + 4\,e^- \rightarrow 2\,OH^- \qquad (3.3)$$

$$2\,H^+ + 2\,e^- \rightarrow H_2 \qquad (3.4)$$

Consequently, a metal loss happens at anodic sites [26, 33]. Fig. 3.2 shows schematic the corrosion of a metal in aqueous environment.

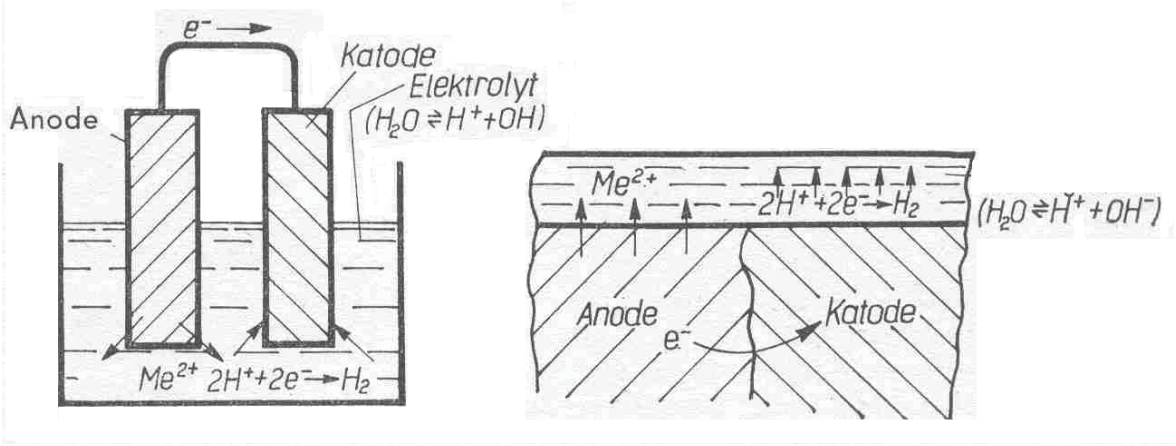

Figure 3.2 Schematic representation of corrosion of a metal in aqueous environment: anodic and cathodic reaction [33].

When a metal is immersed into an electrolyte, a double layer is formed at the metal-solution interface. The most commonly used model of electrical double layer is the Helmholtz model. The "inner Helmholtz plane" adsorbs water molecules and thus hinders contact of reacting ions to electrode surface. At the "outer Helmholtz plane" positive charged metal ions are located at the negative side of the inner Helmholtz layer. The result of this double layer is absolutely analogous to an electrical capacitor, which has two plates of charge separated by some distance (see Fig. 3.3) and hinders mass and charge transport.

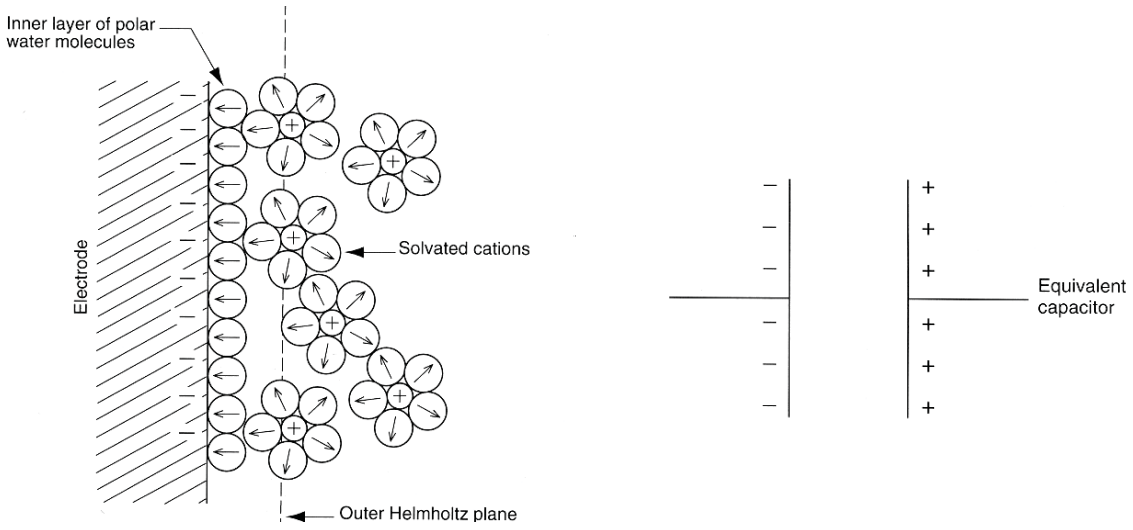

Figure 3.3: Schematic representation of electrical double layer and the equivalent capacitor [34].

3.4. Corrosion Behaviour of Mo an Mo alloys

It is known that Mo provides corrosion properties similar to tungsten and particularly resists non-oxidizing mineral acids. It is relatively inert to carbon dioxide, ammonia, and nitrogen to 1100°C and also in reducing atmospheres containing hydrogen sulfide. Mo offers high heat resistance in a non-oxidizing atmosphere and is easy to etch [1, 2, 35].

Fig. 3.4 shows the Pourbaix diagram for the molybdate system, which presents the thermodynamically stable form of Mo in contact with an aqueous solution containing 1.0 mM molybdenum in the form of MoO_4^{2-} or $HMoO_4^-$, as a function of the applied potential and the pH. The diagram shows the thermodynamically favourable species of Mo as function of pH and potential. Mo shows at acidic pH values a high level of resistance as a result of forming a molybdenum oxide layer. In contrast at the alkaline region Mo occurs as molybdate ion, which has no protective effect.

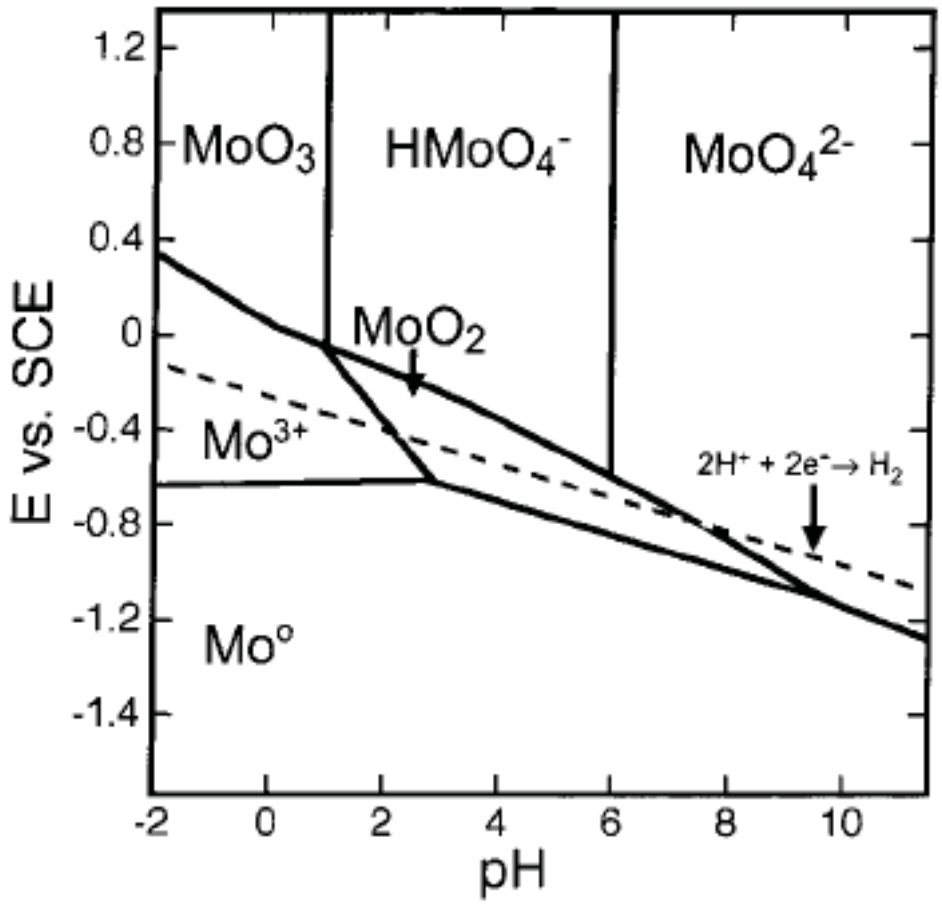

Figure 3.4: The Pourbaix diagram for the molybdate system, which shows the thermodynamically stable form of molybdenum in contact with an aqueous solution containing 1.0mM molybdenum in the form of MoO_4^{2-} or $HMoO_4^-$, as a function of the applied potential and the pH [36].

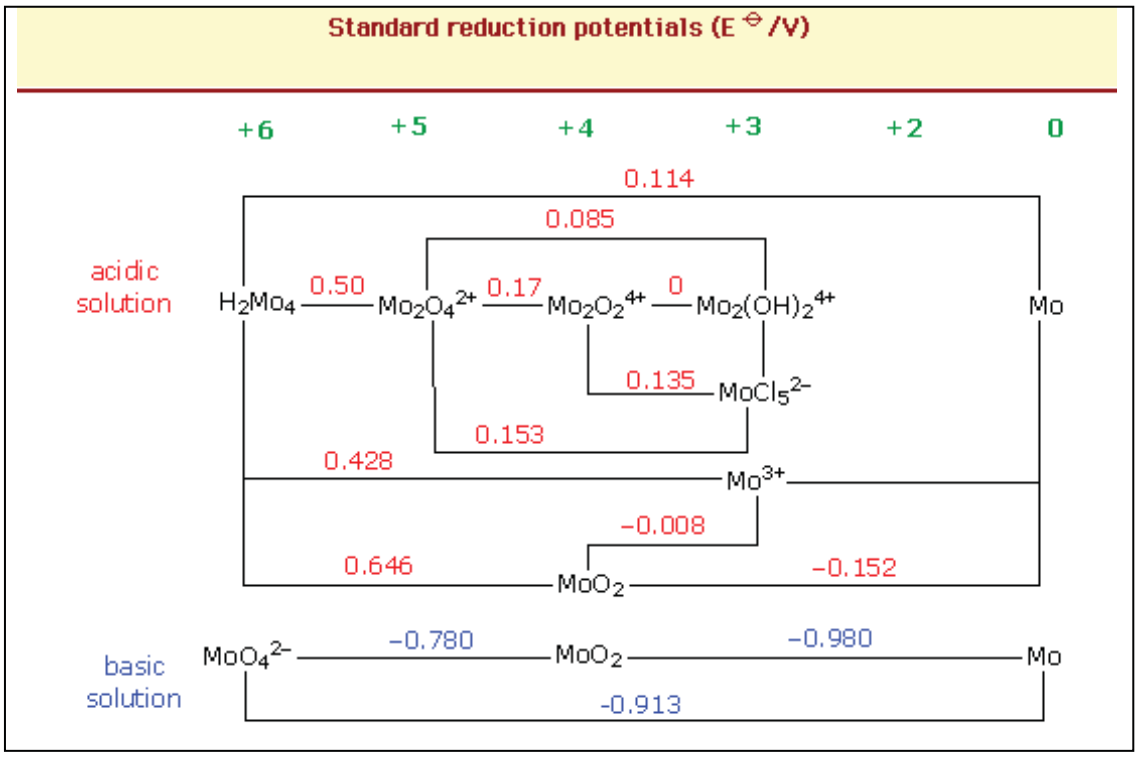

Figure 3.5: Standard reduction potentials of Mo [37].

Additionally the standard reduction potentials of Mo are show in Fig. 3.5. The corrosion potentials of Mo films in acid solutions have more noble values than those of Mo films in neutral solutions and basic solution. This means that the oxide film on Mo is more stable in acid solutions. It is attributed to the relatively low amount of dissolved oxygen in the neutral or basic solution [32].

The corrosion behaviour of molybdenum has been extensively studied by many investigators. Consequently, several studies have been done to improve the low-temperature oxidation and corrosion properties of Mo films. K. Hashimoto et al. [38] have reported spontaneous passivation of sputtered Mo films alloyed with Ta, Zr, Nb, Ti and Cr in concentrated hydrochloric acids (see Fig. 3.6) where all these alloys except Mo-Cr have significantly higher corrosion resistance than that of pure metal. The significant improvement of the corrosion rate is seen at an alloy content in the range between 20 and 80 at.-%.

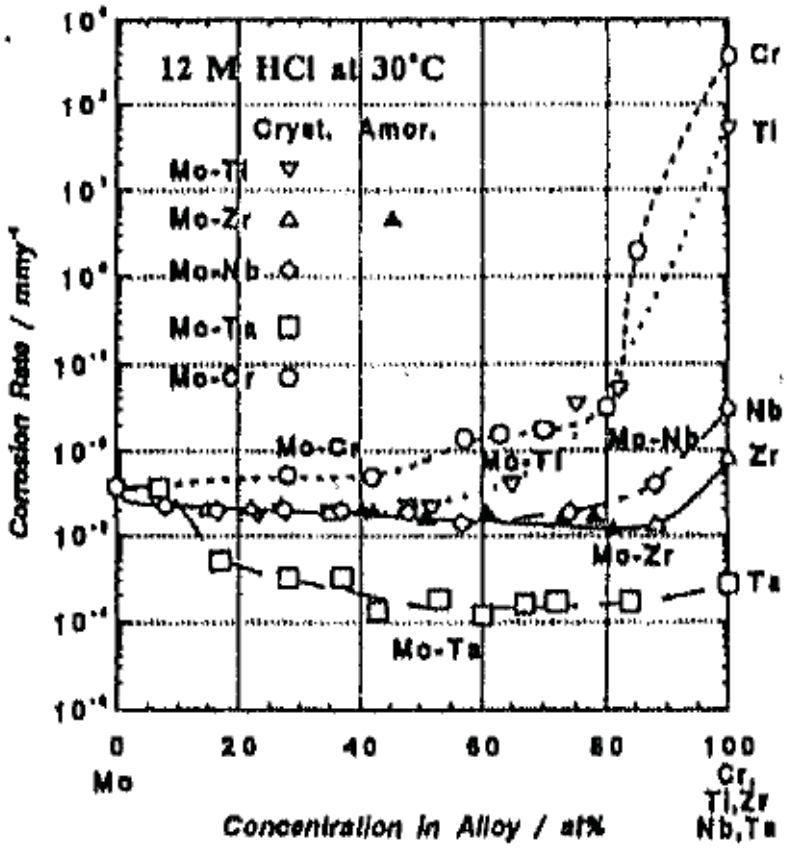

Figure 3.6: Corrosion rates of sputter-deposited Mo alloys, Mo-Ti, Mo-Zr, Mo-Nb, Mo-Ta, Mo-Cr, in 12 M HCL at 30 °C [38]. Significant improvement of corrosion rate is seen at an alloy content in the range between 20 and 80 at.-%.

For the sputter deposited Mo-Ti system Park et al. [39] have reported the formation of highly protective molybdenum-titanium double oxyhydroxide, in which Mo^{4+} ions are linked directly or through O^{2-} ions with Ti^{4+} ions. Fig. 3.7 shows the change in relative amounts of Mo species in air-formed films and spontaneously passivated films, respectively, as a function of alloy composition. In the spontaneously passivated films, the relative amounts of Mo^{4+} ions decrease with the alloy titanium content. The major Mo species in the films on the alloys having lower corrosion rates are always Mo^{4+} ions. The lowest corrosion rates are obtained at a alloy content of ~ 20 at.-% Ti, where the highest amount of Mo^{4+} ions is seen (Fig. 3.7).

lowest corrosion rate for Mo-Ti alloys.

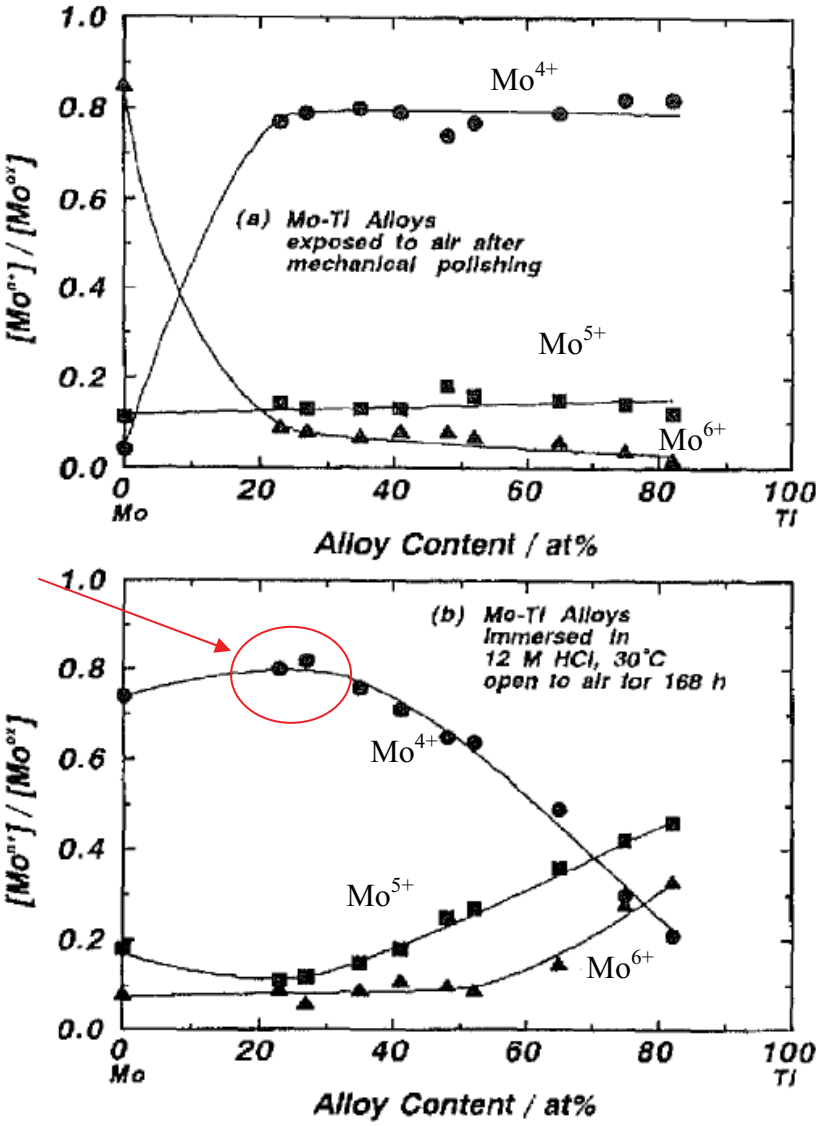

Figure 3.7: Fractions of Mo^{4+}, Mo^{5+} and Mo^{6+} ions in total Mo ions in the air-formed (a) and spontaneously passivated (b) films on sputter-deposited Mo-Ti alloys as a function of alloy titanium content[43]. The red circle indicates the lowest corrosion rate for Mo-Ti alloys at ~20 at.-% Ti, where the highest amount of Mo^{4+} ions is seen.

It has been reported by Hashimoto and al. [40] for binary Cr-Mo alloy, the molybdenum component of the oxide film is considered to be the component of the oxide which promotes passivity in concentrated hydrochloric acids. For this example, a network of Mo-O-Mo bridges in the oxide film first considered and then Cr^{3+} ions are inserted stochastically into the Mo-O-Mo network. The Mo^{4+} species is primarily responsible for the passivity of pure Mo. The pure oxide MoO_2 is octahedral coordinated with six oxygen

ions, and each oxygen ion is coordinated with three Mo^{+4} ions. Fig. 3.8 shows the graph of MoO_2. The Mo^{+4} ions are placed at vertices, and O^{-2} ions are placed at edges.

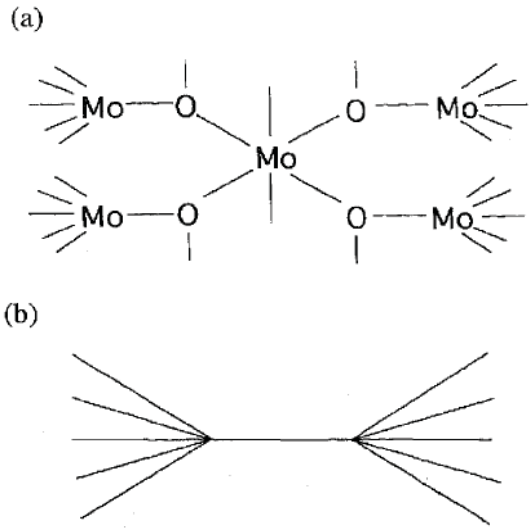

Figure 3.8: (a) Representation of two adjacent MoO_2 octahedra, (b) The Mo atoms (ions) are represented by the edges. There are (2/3) O atoms (ions) per edge [40].

It has been reported that the roles of alloying elements in the passivation of alloys are based on two fundamental properties of metals, namely, the metal-oxygen bond strength and the metal-metal bond strength. Passivation will be enhanced by elements which have a high metal-oxygen and low metal-metal bond energy. Mo corresponds to a strong Mo-Mo bond. [39].

In summary investigations of the oxidation behaviour and the corrosion resistance of sputtered Mo thin films alloyed in wide composition ranges (between 10 and 90 at.-%) in concentrated hydrochloric acids have been done. The lack of a systematic study of the effect of low contents (<10%) of alloying elements in sputter deposited Mo films on their corrosion resistance was the main initiator of present investigations. Since significant improvement of the corrosion rate was seen at an alloy content in the range between 20 and 80 at.-% only small differences in corrosion behaviour are expected at present study.

The present work aims to synthesize Mo thin film alloyed with low contents of Ti, Cr, Ni, Nb, Ta or W, respectively by sputter deposition and to examine the corrosion behaviour of these alloys during exposure in a climatic test chamber and by different electrochemical measurements in 0.9 % NaCl aqueous solution.

4. Experimental

4.1. Coating deposition

4.1.1. Coating facility

For the preparation of all coatings within this thesis, a laboratory-scale unbalanced DC magnetron sputtering device at the Montanuniversität Leoben, as shown in Fig. 4.1, was used. The sputtering set-up was based on a Leybold Univex 300 and consists of a stainless-steel chamber (Ø 300 x 200 mm). There are two parts (see Fig. 4.1), the upper one contains

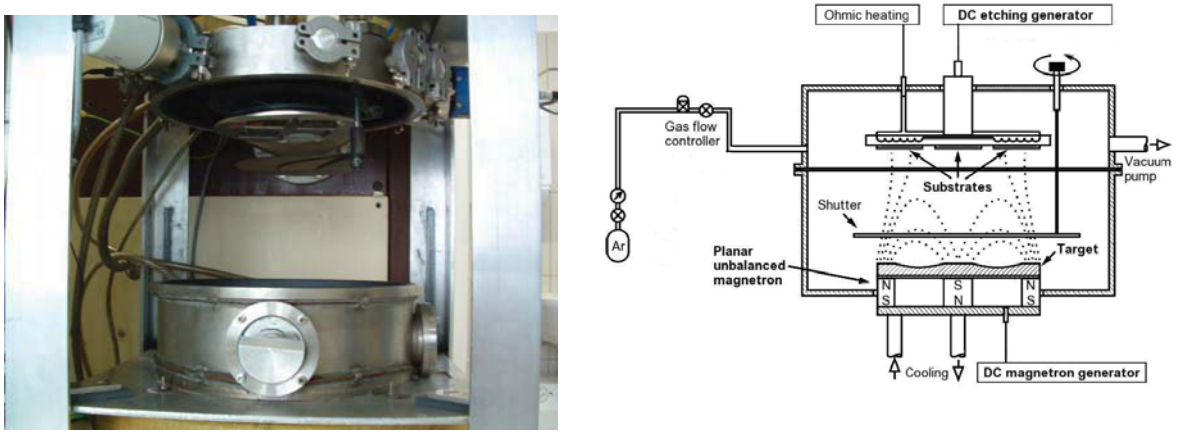

Figure 4.1: The DC sputtering configuration used and a schematic arrangement of deposition plant.

the heated substrate plate, the working gas inlet, the flange to the pumping system as well as the rotable shutter. In the lower part, the water cooled target positioned on a circular unbalanced planar magnetron (Genoca PP150) is located. The chamber can be opened and closed by a vertical movement of the lower part. The two step pumping system consists of a rotary vane vacuum pump (Balzers DUO 016 B) and a turbo molecular pump (Leybold Turbovac TW 250). To apply a negative potential for the substrate etching process, an independent dc Hippotronics 803-330 power supply was used. During the deposition process a negative substrate potential (bias) was supplied by a dc power supply (Heinzinger PTN 350 – 1). The magnetron power supply for sputtering of the target was a dc supply (ENI DCG 75E) and the target-to-substrate distance was 7.5 cm.

4.1.2. Target and Substrates

For deposition of the coatings, a molybdenum target with a purity of 99.97 wt.- % and Ø 152.4 x 6 mm (PLANSEE Metall GmbH) has been used. For deposition of the binary alloyed films, 24 inserts with Ø 5 mm have been placed symmetrically in blind holes over the sputter erosion region of the molybdenum "mosaic" target (see Fig. 4.2). The alloy composition was controlled by changing the small inserts placed on the target. The alloying elements used as inserts were: Ti, Nb, Ta, Cr, W and Ni.

Figure 4.2: Molybdenum "mosaic" target with holes for the alloying-elements-inserts.

Fig. 4.3 shows the configuration used for deposition of the ternary alloys. Three ternary alloy systems, namely Mo-Ta-Ti, Mo-Ta-Nb and Mo-Ti-Nb, were synthesized by arranging the inserts Ti, Nb and Ta in the mosaic target.

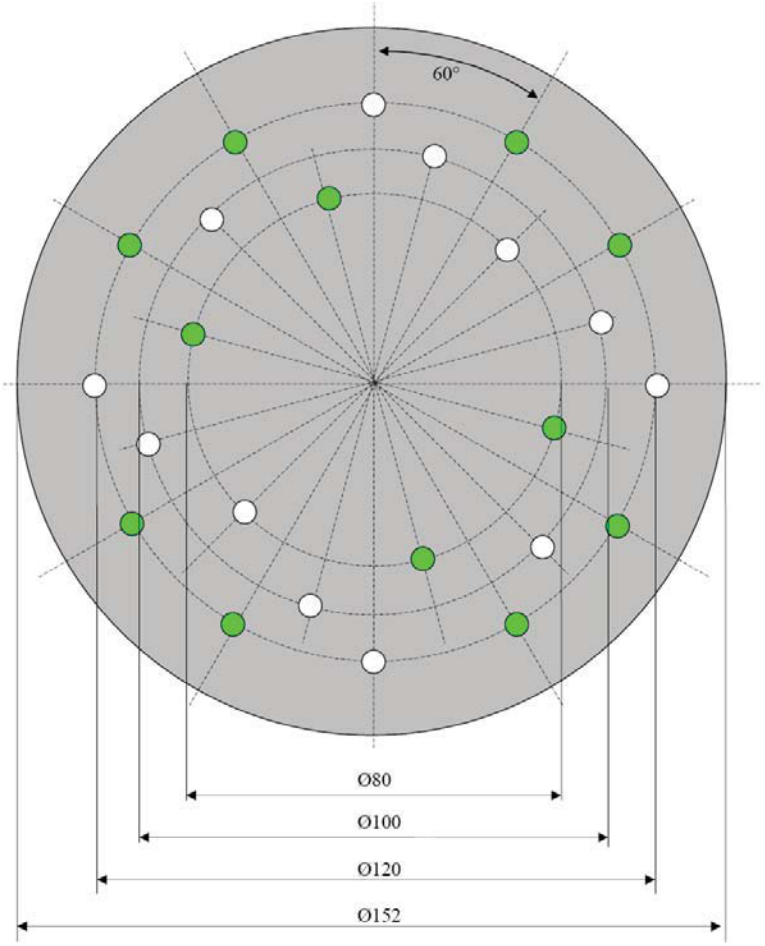

Combination: Mo + X + Y (ternary alloy)

		1	2	3
●	alloying element X:	Ta	Ta	Ti
○	alloying element Y:	Ti	Nb	Nb

Figure 4.3: Schematic illustration of molybdenum "mosaic" target used for ternary alloys.

Coatings were deposited on alkaline earth boro-aluminosilicate glass plates for display technologies type, Corning EAGLE 2000TM AMLCD, of dimension 50.8 x 50.8 x 0.7 mm. The glass sheets have been cleaned by using a commercial detergent from Borer Chemistry for glass cleaning.

4.1.3. Deposition procedure

The deposition procedure includes the following steps:

- Mounting of four cleaned glass substrates in the sample holder onto the substrate plate assembly in the deposition chamber.
- Chamber evacuation by starting the pumping system. Then the substrate holder was heated up to 350° C for 90 minutes to support degassing and desorption processes. After cooling for about 90 min to deposition temperature of 120° C, a base pressure of $\leq 3 \times 10^{-3}$ Pa was reached.
- Sputter cleaning of the target was carried out at a power of 1000 W for 10 minutes in argon atmosphere (flow rate 15 sccm). The shutter located in front of the target was closed in order to avoid substrate contamination.
- Ion etching of the substrates was carried out to clean the surface of the substrates. In argon atmosphere (pressure 3.5 Pa, ~ 200 sccm) a plasma was ignited between the substrates and inserted grounded shutter. The etching voltage was set to –1250 V with a resulting etching current of approximately 10 mA. Simultaneously, target precleaning was continued at minimum power (~ 20 W). After 5 minutes etching, the work gas flow rate was reset to 15 sccm.
- When pressure (0.3 Pa) and temperature (~120°C) reached a constant value, the planar magnetron sputter power was set to 1000 W, and all deposition parameters were adjusted, such as bias voltage (-50 V). Finally, the shutter between target and substrate was opened.
- During the deposition process, the deposition parameters were held constant until an average coating thickness was reached. Deposition time was 100 seconds for ~ 220 nm, 175 seconds for ~ 400 nm and 20 minutes for ~ 2.5 µm thick coatings.
- Cooling down, stopping the pumping system after reaching a temperature below 100°C, venting the chamber and removal of the substrates.

In order to obtain different Mo-alloy films the target inserts have been varied. Table 4.1 shows the deposition parameters for all coating systems.

Table 4.1 Deposition parameters for all coating systems

Alloy system	P_m [W]	U_{bias} [V]	Ar [sccm]	T_{dep} [°C]	time	thickness [nm]
Mo	1000	-50	15	120	20 min	2300
Mo	1000	-50	15	120	3 min	380
Mo-Cr	1000	-50	15	120	20 min	2300
Mo-Cr	1000	-50	15	120	2 min	250
Mo-Ta	1000	-50	15	120	20 min	2300
Mo-Ta	1000	-50	15	120	100 sec	220
Mo-Ti	1000	-50	15	120	20 min	2300
Mo-Ti	1000	-50	15	120	100 sec	220
Mo-Nb	1000	-50	15	120	20 min	2300
Mo-Nb	1000	-50	15	120	100 sec	220
Mo-Ni	1000	-50	15	120	20 min	2300
Mo-Ni	1000	-50	15	120	100 sec	220
Mo-Nb	1000	-50	15	120	20 min	2300
Mo-Nb	1000	-50	15	120	100 sec	220
Mo-W	1000	-50	15	120	20 min	2300
Mo-W	1000	-50	15	120	100 sec	220
Mo-Ti-Ta	1000	-50	15	120	175 sec	400
Mo-Ti-Nb	1000	-50	15	120	175 sec	400
Mo-Ta-Nb	1000	-50	15	120	175 sec	400

4.2. Coating Characterization

4.2.1. Scanning Electron Microscopy

A scanning electron microscope (Zeiss Evo50 SEM) was used to investigate the coating morphology and film thickness on fractured cross-sections. Further, the chemical composition was determined with an attached Oxford Instruments INCA energy-dispersive X-ray analysis device (EDX).

4.2.2. Profilometer

Thickness uniformity of the sputtered films was characterized on the steps of partly masked and thus uncoated substrate areas. A Veeco Wyko NT1000 optical white light profiler, based on the Michelson-interferometer, was used. Fig. 4.4 shows the beam path of an optical profilometer. An interference pattern is produced by splitting a beam of light into two paths. One beam passes through the objective to the sample surface, the other is reflected at the reference mirror within the interferometer. Afterwards, both beams reunite and form an interference pattern which can be detected by a CCD camera [23]. In this work the step height between coated and uncoated areas was measured and as a result the film thickness distributions across the substrate was obtained.

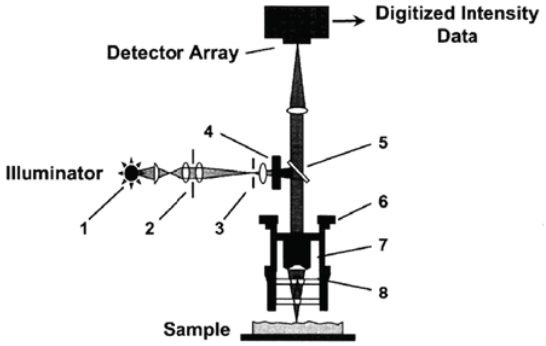

Figure 4.4: Beam path and working principle of the optical profilometer: 1) light source, 2) aperture, 3) field stop, 4) filter, 5) beam splitter, 6) transistor, 7) microscope objective, 8) Mirau interferometer [41].

4.2.3. X-ray Diffraction Analysis

X-ray diffraction (XRD) is a common, non destructive testing method for structural analysis and evaluation of residual stresses and grain size. The diffraction patterns result from reflection of X-ray radiation at lattice planes of crystallites. Most of these reflections are destructive, constructive interference only occurs if Braggs law is fulfilled [42]:

$$n \cdot \lambda = 2 d_{hkl} \cdot \sin\theta \qquad (4.1)$$

There, λ is the wavelength of the radiation, d_{hkl} is the interplanar spacing of a lattice plane with the Miller indices h, k and l and θ designates the diffraction angle.
The measurements were carried out by using a Bruker-AXS D8 Advance diffractometer with Cu Kα ratiaton in Bragg-Brentano geometry (see Table 4.2 and Fig. 4.5). The sample

is irradiated at an angle θ, while the diffracted beam is detected at an angle 2θ with respect to the incident beam. This is called a θ-2θ scan, the sample rotates at half angular velocity with respect to the detector. In this geometry, only lattice planes with the plane normal parallel to the beam are measured. Every detected reflection may be connected to the crystalline structure of a known chemical element or compound. The identification of the characteristic peaks was done by JCPDS (joint committee on powder diffraction standards) files.

Table 4.2 Parameters for XRD measurements

λ Cu Kα [nm]	High Voltage [kV]	Tube Current [mA]	Step Time [s]	2θ [°]	2θ range [°]
0.154056	40	40	1.2	0.02	20-120

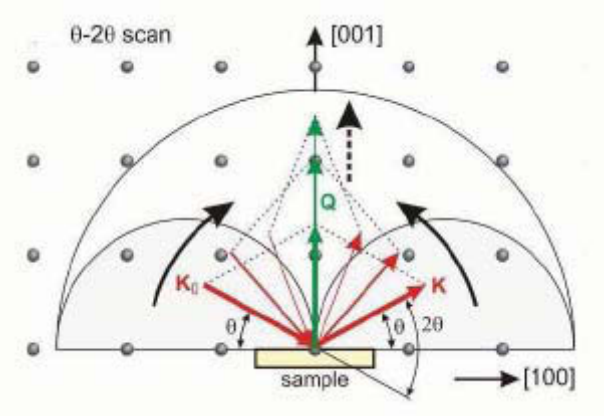

Figure 4.5: Schematic drawing of θ-2θ scan [43].

Additional useful information about the crystal is given by the position of the peak and its broadening. The latter is related to grain size and inhomogeneous strain, resulting in the so called microstress. The microstress is caused by coating defects such as vacancies or interstitials, which result in interplanar spacing variations. A deviation of the peak position from its standard position shows the presence of uniform stress, so called macrostress [44, 47]. The peak profile strongly depends on micro strain (described by a Gaussian function) and grain size (described by a Cauchy function). Therefore, a linear combination of Cauchy and Gaussian functions, i.e. the so called Pseudo-Voigt function is used to fit the XRD profiles [17].

4.2.4. Electrical Resistance

The measurement of the electrical resistance was performed with a MDC Multi Height Probe system. The measurement of area resistance is the principle of this system. It consists of a 4-point probe station (4 equal tungsten tips), an ampere meter, a dc current source and a voltmeter. The four probes are arranged in a linear fashion, where the two outer probes are connected to a current supply, and the inner probes to a voltage meter (see Fig. 4.6). As current flows between the outer probes, the voltage drop across the inner probes is measured. The relationship of the current and voltage values depends on the resistivity of the measured material and is calculated by [45]:

$$\rho = \frac{\pi \cdot t_c}{\ln 2} \cdot \frac{U}{I} \tag{4.2}$$

There, t_c is the coating thickness, U is the measured voltage and I is the adjusted current. The electrical conductivity σ is calculated by [46]:

$$\sigma = \frac{1}{\rho} \tag{4.3}$$

Important for this measurement is that the current is driven through the coating. This is possible by using a substrate with a higher electrical resistance than the coating.

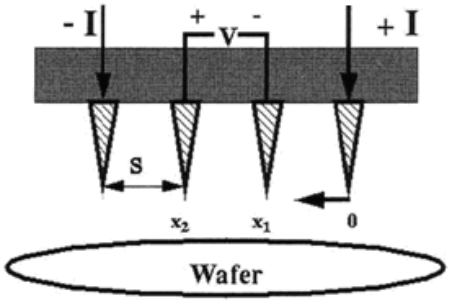

Figure 4.6: Schematic image of the electrical resistance measurement [45].

4.3. Corrosion Properties

All samples have been stored at least for 1 week on air at room temperature to allow development natural oxide-films. For studying the corrosion behaviour three different techniques have been used (potentiodynamic polarisation, impedance spectroscopy and

exposure testing). For characterization of the corroded surfaces, X-ray photoelectron spectroscopy (XPS) and Raman spectroscopy were performed.

4.3.1. Potentiodynamic Polarisation

The polarization behaviour of Mo and Mo alloy films was measured in a 0.9% NaCl aqueous solution at room temperature and a saturated calomel electrode (SCE) with a potential of 241 mV_{SHE} (standard hydrogen electrode) as reference electrode. Potential was scanned with 600 mV/h and reverse potential was 200 mV_{SCE}. Before starting polarisation the open circuit potential (OCP) was measured for 30 min. The starting potential was 100 mV lower than final OCP. The experimental configuration is shown in Fig. 4.7.

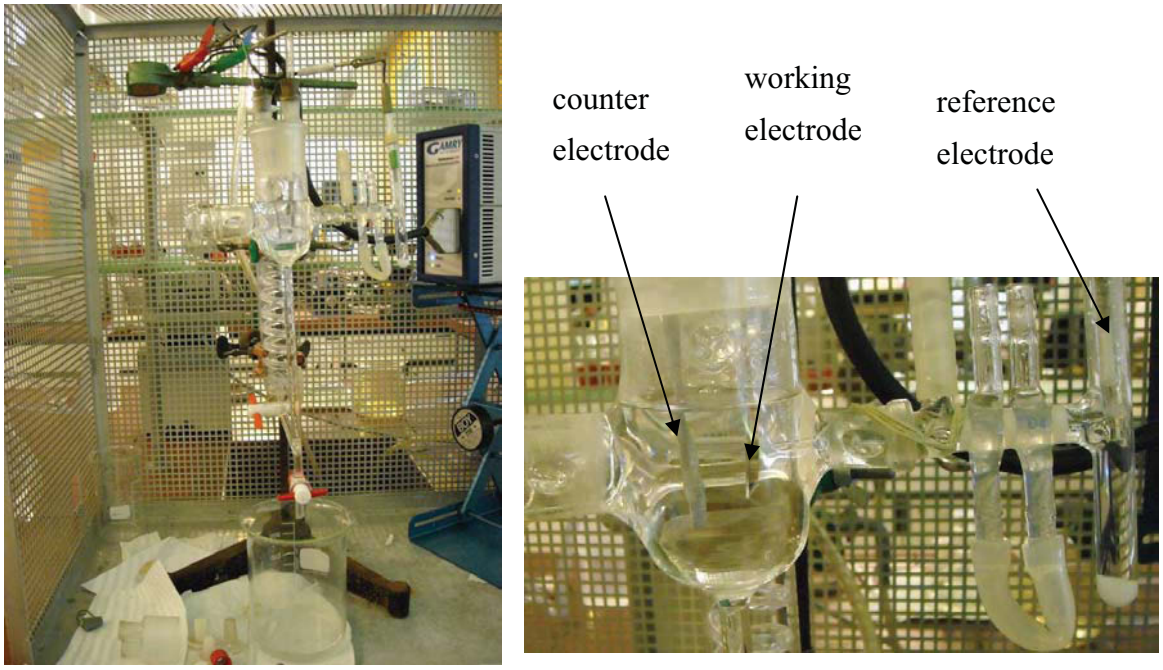

Figure 4.7: Experimental configuration used for potentio-dynamic polarisation, (a) electrochemical cell, (b) Electrode setup in electrochemical cell

Fig. 4.8 shows schematically a polarisation curve. From this curves corrosion potential (E_{corr}) and by Tafel extrapolation the corrosion current density (i_{corr}) were determined. Corrosions rates (r) were calculated as follows [34]:

$$r = \frac{I_{corr} \cdot MG}{z \cdot F \cdot \rho} \tag{4.4}$$

There MG is the molecular weight, z is the number of electrons, F is the Faradaic constant and ρ is the density of molybdenum.

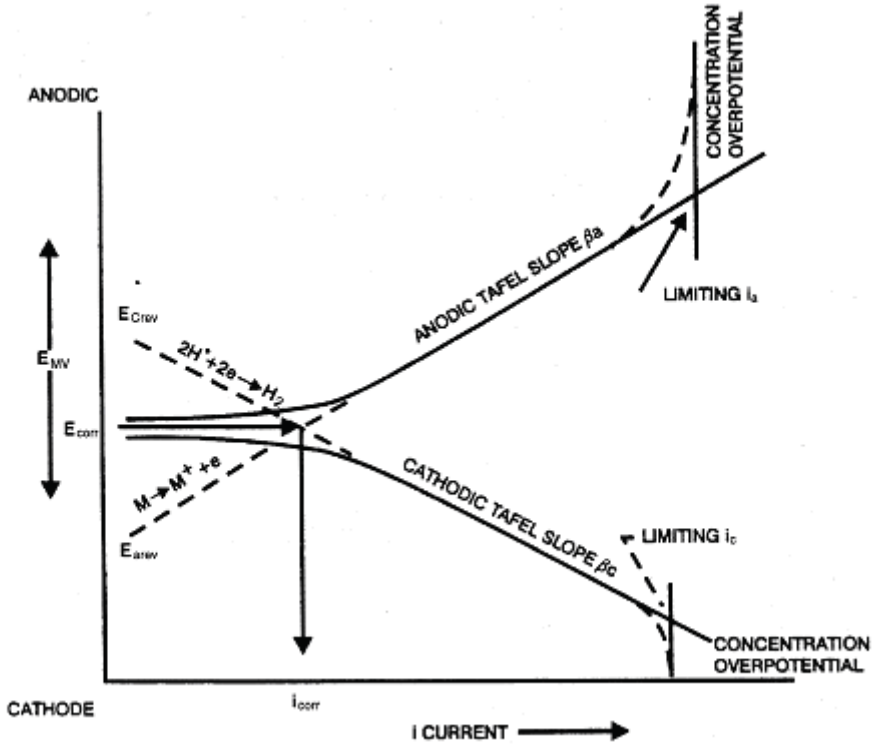

Figure 4.8: Schematic polarisation curves showing the pertinent process for the metal/solution [5].

4.3.2. Electrochemical Impedance Spectroscopy

Here, as for traditional polarisation experiments a three electrode technique is used, a corroding working electrode (Mo and Mo alloy films), a counter electrode made of platinum (Pt) and the SCE as reference electrode. Between working electrode and SCE an alternating voltage (V) is applied and the frequency is modulated as follows [34]:

$$V(t) = V_0 \cdot \sin \omega t \tag{4.5}$$

Here t is the time and $\omega = 2\pi f$ (f is the frequency).

Impedance measurements were performed by application of a tube cell onto the specimens surface as shown Fig. 4.9. The measurements were carried out 0, 4 and 24 h after

immersion into the in a 0.9% NaCl test solution at room temperature. Alternating voltage was ± 10 mV and a frequency range between 1 mHz and 500 kHz has been investigated.

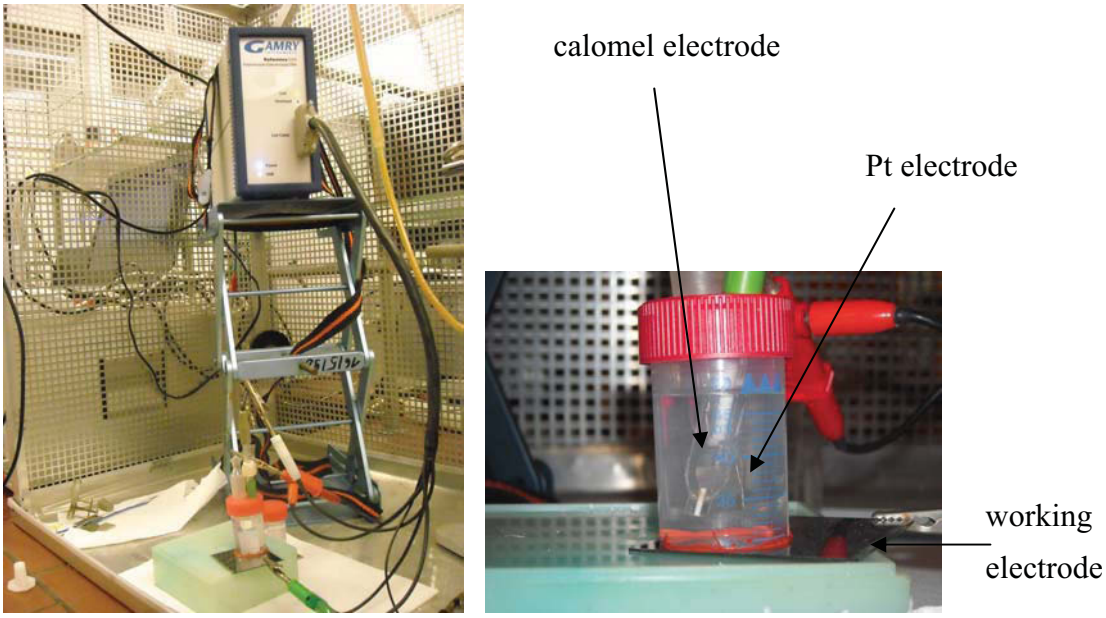

Figure 4.9: Experimental setup used for electrochemical impedance spectroscopy, (a) Potentiostat with cell, (b) Detail of cell.

The corroding electrode (probe) can be described by an equivalent circuit model. The simplest electrode contains (see Fig. 4.10): a double layer capacity (C), a polarisation resistance (R_P) and an ohmic resistance (R_Ω) representing resistance of the electrolyte.

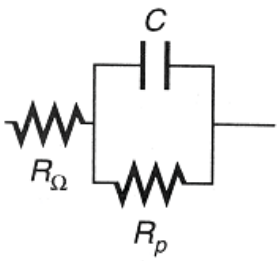

Figure 4.10: Equivalent circuit, where C is the double layer capacity, R_P the polarisation resistance and R_Ω the ohmic resistance [34].

From alternating voltage results an alternating current results with a phase shift (Θ):

$$I(t) = I_0 \sin(\omega t + \Theta) \qquad (4.6)$$

Voltage and current are related to each other via the complex impedance (Z):

$$Z(\omega) = \frac{V_0}{I_0} \qquad (4.7)$$

The impedance (complex resistance) consists of a real and an imaginary part. For evaluation of data, the polarization resistance was calculated from Nyquist plots (see Fig. 4.11). R_P represents the corrosion rate of the alloy at OCP. The higher R_P the better is the corrosion behaviour. In other words, the lowest polarisation resistance is equal to the highest corrosion rate [5, 34].

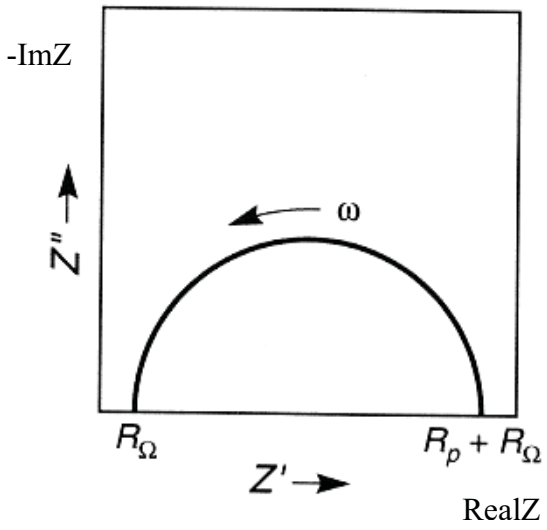

Figure 4.11: Nyquist plot schematically complex plane Z_i is drawn as function of Z_r, $Z(\omega)=Z_r(\omega)+ i*Z_i(\omega)$ [34].

4.3.3. Exposure Test

Exposure tests were done in a climatic test chamber at 85 % relative humidity and 85°C for 168 h (1 week). The mass gain was measured by weighing the sample before and after exposure to the corrosive environment.

4.3.4. Raman Spectroscopy

Raman spectroscopy of the corroded film surfaces was done by using a Jobin Yvon LabRam confocal Raman spectrometer (see Fig. 4.12) equipped with a frequency-doubled Nd-YAG laser (power, 100 mW; wavelength 532.2 nm). Raman spectroscopy is a widely used non-destructive and non-quantitative method for getting an overview of bonding structure of molecules. It was discovered by Krishna and Raman in 1928 and can be understood as inelastic scattering of photons with molecules [48].

Figure 4.12: Jobin Yvon LabRam confocal-Raman Spectrometer [49]

When monochromatic light is scattered by molecules, a small fraction of the scattered light is observed to have a frequency different from that of the irradiating light and this is known as the Raman effect. The Raman effect occurs when monochromatic light passes through a sample containing molecules that can undergo a change in molecular polarizability as they vibrate, that means coupling between optical and molecule or lattice vibration. Depending onto whether the molecule involved was in an excited vibrational state ore not, scattering of an incident photon results in a loss or gain of energy, leading to Stokes or anti-Stokes Raman scattering. Raman shift frequencies are usually expressed in wave numbers because they correspond directly to the frequencies of vibration and rotation of the atoms within the molecule [48, 56].

4.3.5. X-Ray Photoelectron Spectroscopy

In X-ray photoelectron spectroscopy (XPS) the sample is irradiated with a beam of monochromatic soft X-rays under ultra vacuum conditions. Photo ionisation then takes place on the sample surface. A spectrometer is measuring the kinetic energy (E_k) of the

ejected photo electrons, which is related to the X-ray energy (hν) and the binding energy E_b by Einstein relation [46]:

$$E_k = h\nu - E_b \qquad (4.8)$$

From the number of emitted electrons at certain residual energy, information about bonding and involved elements can be obtained. XPS was applied to analyse the corroded film surfaces using an Omicron Multiprobe system with a monochromised Al Kα beam of 1486.7 eV. The samples had been measured directly on the surface and at a depth of ~50 nm after 45 min sputtering the surface with argon ions. The resulting core level spectra where fitted with Unifit version 2002.

5. Results and Discussion

5.1. Coating Thickness

The first steps of the present work were to deposit thin Mo films with low contents of the alloying elements Ti, Cr, Ni, Nb, Ta or W, respectively. The coating thickness was characterized using SEM on fractured cross-sections (see Fig. 5.1) and the corresponding film growth rate was calculated to ~ 2.1 nm/sec. Thus, the sputter time was set to 100 sec for 220 nm, 175 sec for 400 nm and 20 min for 2.5 µm films. The film growth rate was not significantly affected by the alloying elements.

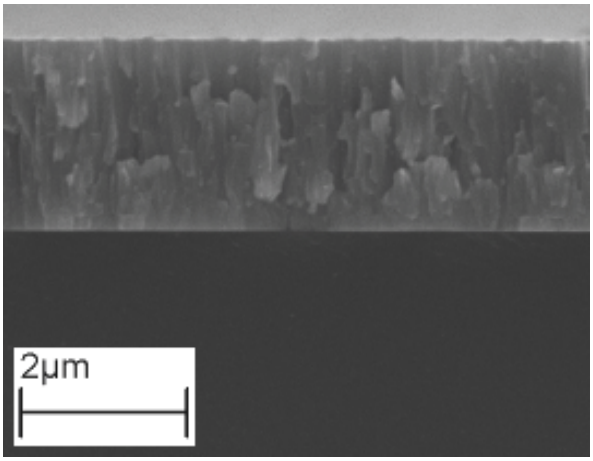

Figure 5.1: SEM fracture cross-section of a molybdenum film sputtered for 20 min.

The coating uniformity was evaluated using the profilometer. As shown schematically in Fig. 5.2, the steps of partly masked and thus uncoated substrates areas were measured along the arrows. The thickness was in the range between 230 nm (close the onset of the arrow) and 150 nm (arrowhead).

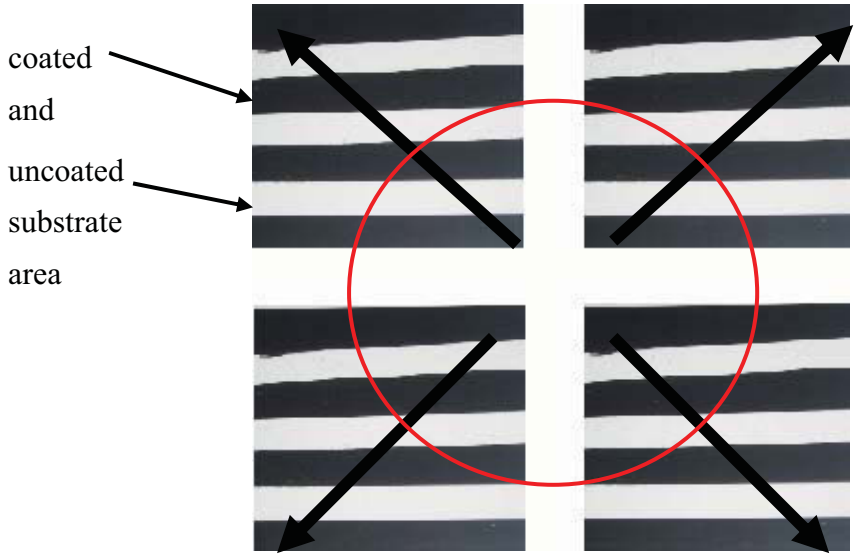

Figure 5.2: Four partly uncoated substrates for uniformity evaluation are shown as mounted in the vacuum chamber. Along the arrows the step-height was measured. The parts inside the circle were indentified as homogeneous.

The uniform part was identified over the target racetrack area within the red circle (see Fig. 5.2), and with a film thickness range of 220 ± 10 nm. For all experiments, this homogeneous part of the coatings was considered.

5.2. Chemical Composition

The chemical composition of the coating was measured by energy dispersive X-ray spectroscopy (EDX) of the thicker (2.5 µm) films. The ternary alloys had not been measured by EDX because the low content of each alloy component is not detectable. Fig. 5.3 shows the Mo alloy film systems, with a schematic illustration of the four coated substrates and respective measurement points with the determined alloy content. The alloying content was in the range between 3.2 und 5.2 at.-%. It has to be noted, that Mo and Nb peaks overlap in EDX, giving rise to a higher uncertainty in determining the Nb content.

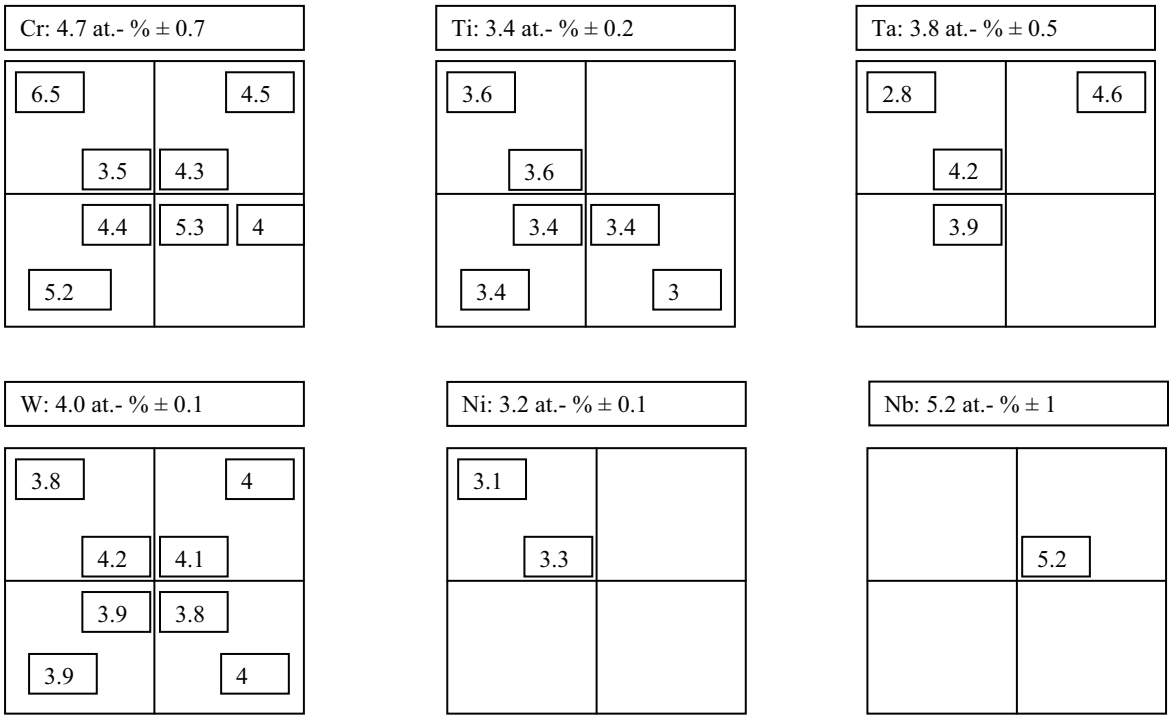

Figure 5.3: Schematic of the measurement principle for determining of the alloy content. The four symmetrically placed squares represent the substrate plate assembly, the small rectangles the measurement points with the detected alloy content and above the substrates the mean alloy content is given. The obtained values were in the range between 3.2 und 5.2 at.-%. There is a higher uncertainty in determining the Nb content because Mo and Nb peaks overlap in EDX.

In order to help understanding the origin of the chemical composition of the films derived from the EDX analyses, additional process simulations were performed. The efficiency of sputtering at the target was simulated using a Monte Carlo algorithm based on TRIM (Transport of Ions in Mater) [50]. The used SRIM code (Stopping and Range of Ions into Matter) is based on a full quantum mechanical treatment of ion-atom collisions. The program utilizes the binary collisions approximation. A full description of the calculation and the program package can be found in Refs. [50-52]. Here simulation was performed by calculating 1000 argon ions incident perpendicular to the surface of the target with an energy of 500 eV. Simulation was made separately with Mo, Ti, Cr, Ni, Nb, Ta and W as target material. Fig 5.4 shows the results of a SRIM simulation for Mo as target.

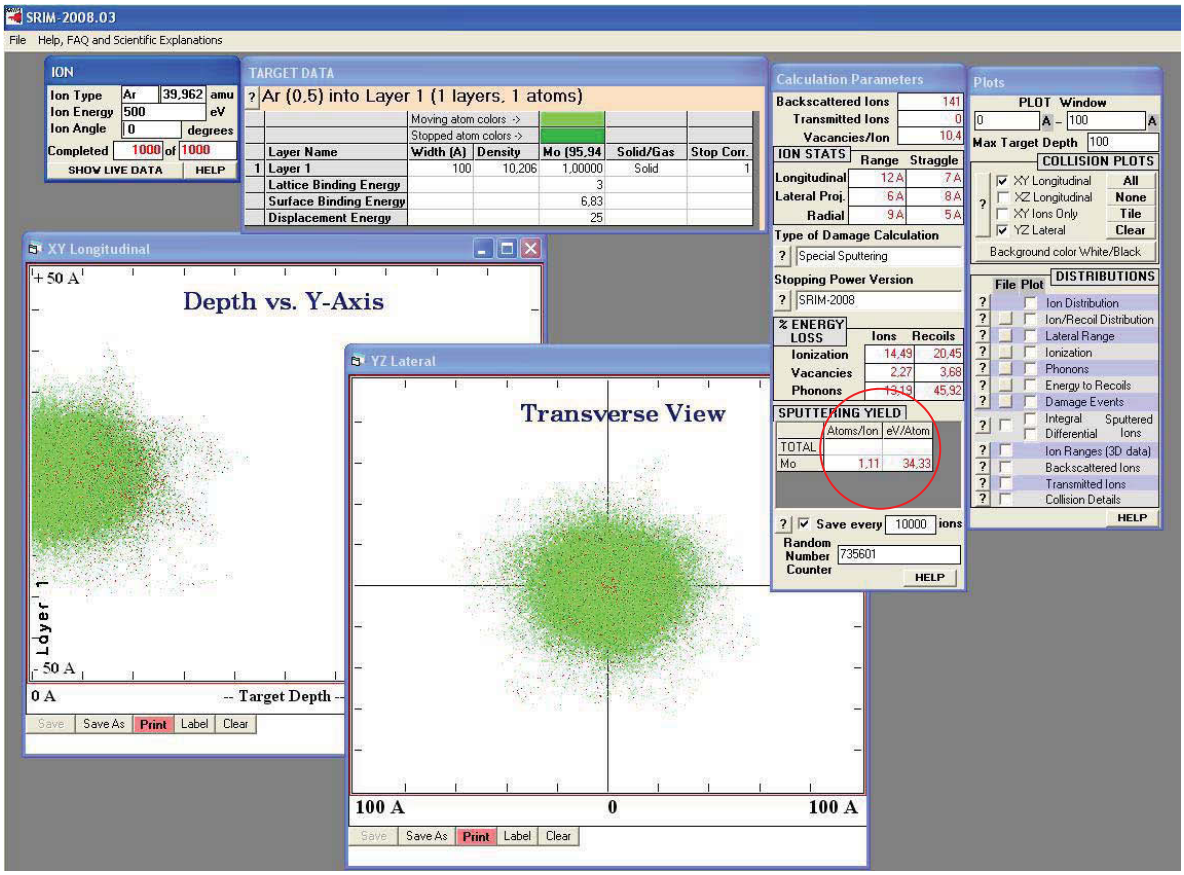

Figure 5.4: Screenshot of a SRIM calculation showing the collision cascades and calculation as well as the data outputs. The red circle indicates the data relevant for this thesis, i.e. the sputter yield given in atoms/ ions and the kinetic energy of the sputtered atoms given in eV/atom.

For estimation of thermalization of energetic species sputtered from the target, the scattering characteristics during the transport phase from the target to the substrate was characterized by the energy transfer coefficient ε [22]:

$$\varepsilon = \frac{4 \cdot m_1 \cdot m_2}{(m_1 + m_2)^2} \tag{5.1}$$

There, m_1 is the mass of atoms sputtered from the target and m_2 is the mass of argon. The results of the SRIM calculation (sputter yield, energy per sputtered atom) and the energy transfer coefficient are listed in Table 5.1.

The alloying content was, as shown in Fig. 5.3, in the range between 3.2 und 5.2 at.-%. To understand the differences between the used alloying elements it is helpful to compare the different sputter yields and scattering characteristics (see Table 5.1). The value of sputter yield in atoms/ions shows how efficient the element is sputtered compared to Mo. If the

value is higher than for Mo, the flux of sputtered species initially leaving the mosaic target shows high element concentration. A high energy transfer coefficient, defined by the atom mass comparable to Ar, indicates quick thermalization of sputtered atoms. For Ti the lowest alloying content was obtained. This is in good agreement to the calculated low value for the sputter yield. Consequently, for the Mo-Ti system the flux of sputtered species leaving the mosaic target shows a lower alloying element concentration as compared to the target composition in the erosion track. Also a high energy transfer coefficient was obtained for Ti and thus a number of sputtered Ti atoms do not reach the substrate, explaining the relatively low alloying content of the coating. On the other hand, significantly higher alloying concentrations are observed for Cr with a high sputter yield as well as for Ta and W with also relatively high yields. In addition, high energies per sputtered atom and low energy transfer coefficients are found. However, while for Ti, Cr, Ta and W SRIM results are in excellent agreement with coating composition derived from EDX analyses, Nb with a relatively low sputter yield but high alloying content does not seem to follow these arguments. The reasons for the high Nb alloying content are presently unclear, and it has to considered that the Mo and Nb peaks overlap in EDX, giving rise to a higher uncertainty in determining the Nb content. Otherwise, Ni with the highest sputter yield observed shows a relatively low concentration, which might be due its ferromagnetic nature providing a short-circuit for the magnetic field lines of the magnetron. Moreover it has to be mentioned, that the likely different condensation behavior of the individual atoms at the substrate has not been considered, due lacking literature data.

Table 5.1. Summary of investigated Mo alloy film systems with their respective alloying content, atomic mass, sputter yield, energy per sputtered atom and energy transfer coefficient.

Alloying element	Alloying content [at.-%]	Atomic mass	Sputter yield	Energy per sputtered atom [eV]	Energy transfer coefficient
Mo	100	96	1.11	34.3	0.83
Ti	3.4 ± 0.2	48	0.64	28.1	0.99
Cr	4.7 ± 0.7	52	1.43	18.3	0.98
Ni	3.2 ± 0.1	59	1.97	21.0	0.96
Nb	5.2 ± 1	93	0.77	40.9	0.84
Ta	3.8 ± 0.5	181	0.96	29.7	0.59
W	4.0 ± 0.1	184	1.04	31.8	0.59

5.3. Microstructure

Fig. 5.5 and Fig. 5.6 show XRD patterns of Mo and Mo alloy film systems, whereas Table 5.2 shows the results of binary and ternary film systems. All coatings deposited show the typical body-centered cubic structure corresponding to well-defined peaks of the Mo phase (2Θ= 40.50°, 58.61°, 73.67°, 87.62°), indicating the formation of single-phase Mo-based solid solutions for all alloying elements. This is attributed to the film growth conditions in magnetron sputtering, which are far away from the thermodynamic equilibrium [27]. Because of the low alloying content in the range between 3.2 and 5.2 at.-%, no peaks for the alloying elements where found.

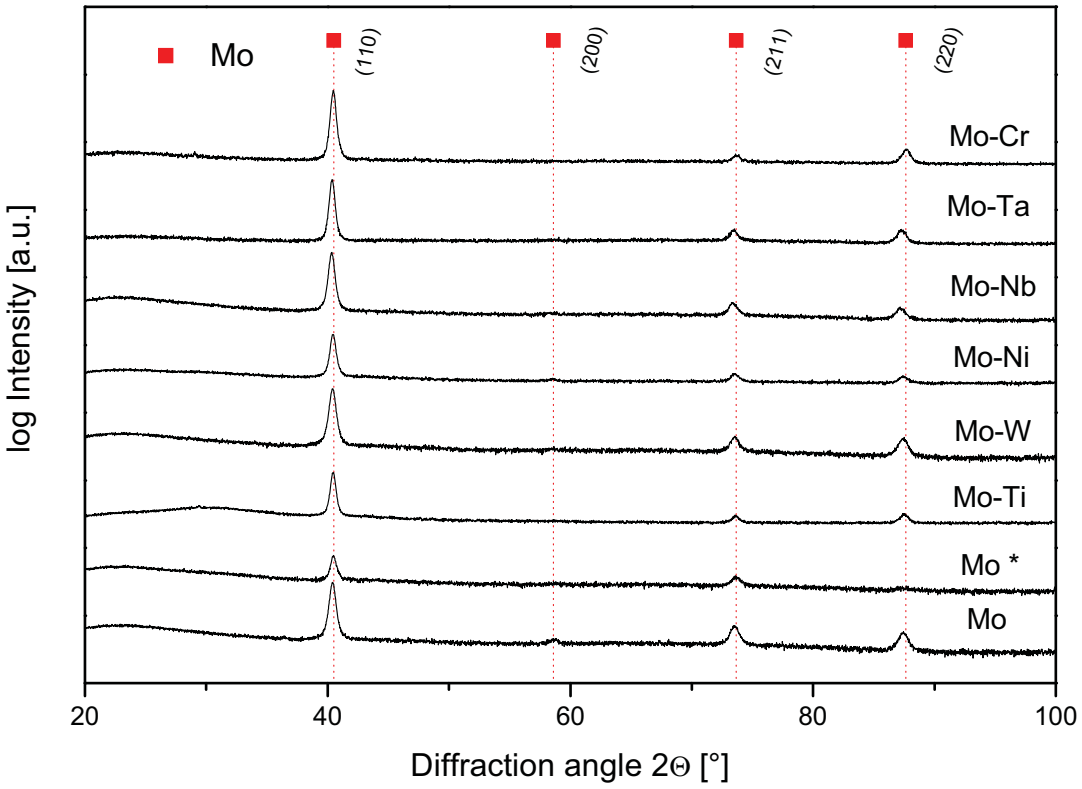

Figure 5.5: XRD patterns of Mo and Mo alloy thin film (~220 nm) systems investigated.

Mo*… Mo after potentiodynamic polarisation

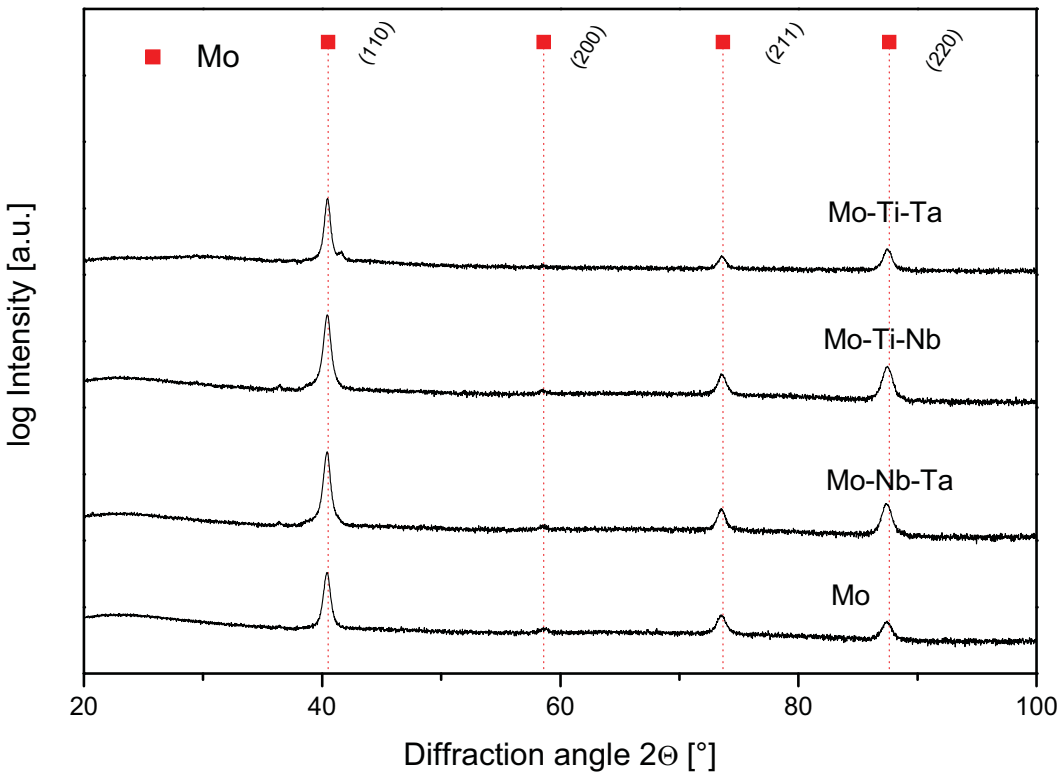

Figure 5.6: XRD patterns of Mo (~220 nm) and Mo ternary alloys (~400nm) film systems.

Fig. 5.5 and Fig. 5.6 let obviously see that there are only small differences in the peak positions of the individual films. Table 5.2 summarizes more detailed analyses of the results of all investigated alloy systems, where the macro-strain was calculated from the XRD peak shift of the (110) peak and the micro-strain from the broadening of the (110) peak using a Pseudo-Voigt fitting function. No significant effect of the alloying elements on the grain size was observed. Due the replacement of Mo atoms by smaller or almost similar-sized atoms as Cr, Ni and W, the lattice parameter increases, and consequently, the peaks shift to higher 2Θ angles. Therefore macro-strains which are lower than those of the unalloyed Mo film are received. For the larger atoms Nb and Ta the peaks shift to lower 2Θ angles and consequently higher macro-strains are obtained. As expected for the micro-strain induced by the element Cr lower values and for the elements Nb and Ta higher values than those of unalloyed Mo films are achieved. While the effect of lattice distortion is well suited to explain the strain generated by alloying of Mo films with most of the

investigated elements, Ti does not seem to follow this trend. Here, the larger sized atom Ti should increase the lattice parameter and should result in higher micro and macro-strains compared to the unalloyed Mo film. But Mo-Ti exhibits the opposite behaviour and lower values are obtained. This may be explained by the fact that Ti is the only alloying element with hexagonal structure.

In the investigated ternary alloys, Mo is replaced through a combination of the elements Ti-Nb, Ta-Nb and Ti-Ta. Here, since these atoms are larger compared to Mo, higher values for micro and macro-strains are expected, but the opposite characteristics are seen. However, this simple interpretation does not consider that for solid solutions also the change in elastic properties and the chemical interaction between the individual atoms have to be taken in account.

Table 5.2: Summary of investigated alloying systems with the atomic radius of respective alloying element, the film grain size, the diffraction angle 2θ of the (110) XRD peak, the determined lattice spacing, the micro-strain and the macro-strain.

Alloy system	Atomic radius [pm]	Grain size [nm]	$2\theta_{(110)}$ [°]	Lattice spacing [nm]	Macro-strain	Micro-strain
Mo	136	42	40.41	0.2230	0.00223	0.00279
Mo-Ti	144	37	40.48	0.2226	0.00057	0.00233
Mo-Cr	125	45	40.53	0.2224	-0.00061	0.00263
Mo-Ni	125	43	40.44	0.2229	0.00152	0.00293
Mo-Nb	142	37	40.33	0.2234	0.00413	0.00295
Mo-Ta	143	48	40.37	0.2232	0.00318	0.00288
Mo-W	137	54	40.49	0.2226	0.00033	0.00261
Mo-Ti-Nb	144/142	56	40.43	0.2229	0.00175	0.00264
Mo-Ta-Nb	143/142	61	40.41	0.2230	0.00223	0.00267
Mo-Ti-Ta	144/143	56	40.45	0.2228	0.00128	0.00225

5.4. Electrical Resistance

The electrical resistance of coatings deposited on glass substrates was measured by the previously described four-point technique (see chapter 4.2.4). The demand on the films was a maximum electrical residence of 15 μΩcm. Table 5.3 shows the electrical resistance of all coating systems. The resistivity of the unalloyed Mo film agrees well to literature data [22, 53, 54]. While the alloying elements Ti, Cr, Nb, Ta and W cause only a slight

increase of the resistivity according to the formation of a Mo based solid solution, the addition of Ni results in an about three times higher resistivity. A reason for this may be that the system Mo-Ni is immiscible as a solid and the lattice might thus be more disturbed than at the other systems.

Table 5.3: Summary of determined electrical resistivity of the films.

Alloy system	Electrical resistivity [μΩcm]
Mo	11
Mo-Ti	15
Mo-Cr	14
Mo-Ni	33
Mo-Nb	14
Mo-Ta	14
Mo-W	12
Mo-Ti-Ta	14
Mo-Nb-Ta	11
Mo-Ti-Nb	12

5.5. Potentiodynamic Polarisation Behaviour

The electrochemical behavior of Mo and Mo alloy films was measured by the previously described potentiodynamic polarization technique (see chapter 4.3.2) in a 0.9 % NaCl aqueous solution. Fig. 5.7 exhibits some samples after the measurement, they show brownish and blue colours.

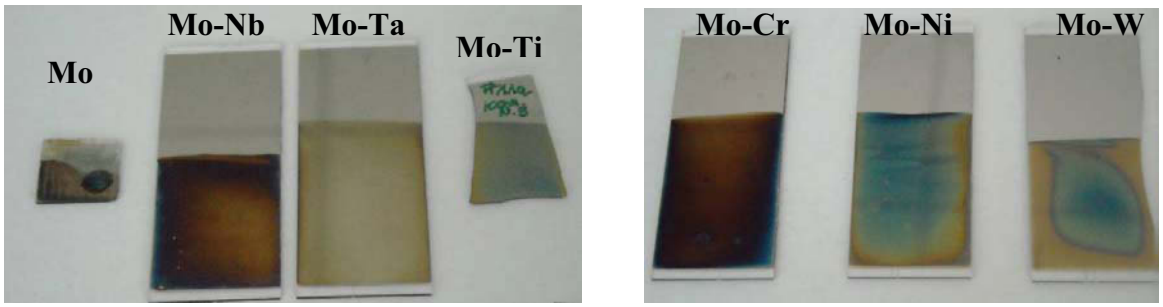

Figure 5.7: Samples after electrochemical measurement with brownish and blue colours.

First three identical samples of Mo-Cr system have been investigated to determine repeatability of results. Scatter of corrosion potential at -270mV was 40 mV_{SCE} and of current density at 0.13 was 0.03 $\mu A/cm^2$ (Fig. 5.8). The potentiodynamic polarization curves of investigated alloys (see Figs. 5.9 to 5.11) show that there are only small differences between different alloys regarding potential and corrosion current density. All corrosion current densities of alloyed samples are lower when compared to Mo (see Table 5.4). The values for films alloyed with W, Ta and Ti are only slightly lower than that of Mo. The best performance show Mo films alloyed with Cr and Ni. The cathodic polarization curves of all alloys are similar to molybdenum. In contradiction the anodic polarization curves show beginning of a passive behavior for Mo-Nb, Mo-Ta and for the ternary alloys. Since passivation occurs only at rather high potentials it is not relevant for this study.

Table 5.4: Corrosion current densities and ranking of the investigated alloy thin film systems.

Alloy system	**Corrosion current density [$\mu A/cm^2$]**	**Ranking**
Mo	0.26 ± 0.03	
Mo-Ti	0.24 ± 0.03	
Mo-Cr	0.13 ± 0.03	
Mo-Ni	0.13 ± 0.03	Mo-Cr, Mo-Ni
Mo-Nb	0.17 ± 0.03	Mo-Nb, ternary alloys
Mo-Ta	0.24 ± 0.03	Mo-Ti, Mo-Ta
Mo-W	0.24 ± 0.03	Mo-W, Mo
Mo-Ti-Ta	0.15 ± 0.03	
Mo-Ti-Nb	0.16 ± 0.03	
Mo-Nb-Ta	0.17 ± 0.03	

Although the scatter of corrosion potential is almost in the same order of magnitude as the differences measured for various alloys, Cr and Ni show improved corrosion properties when compared to other alloys.

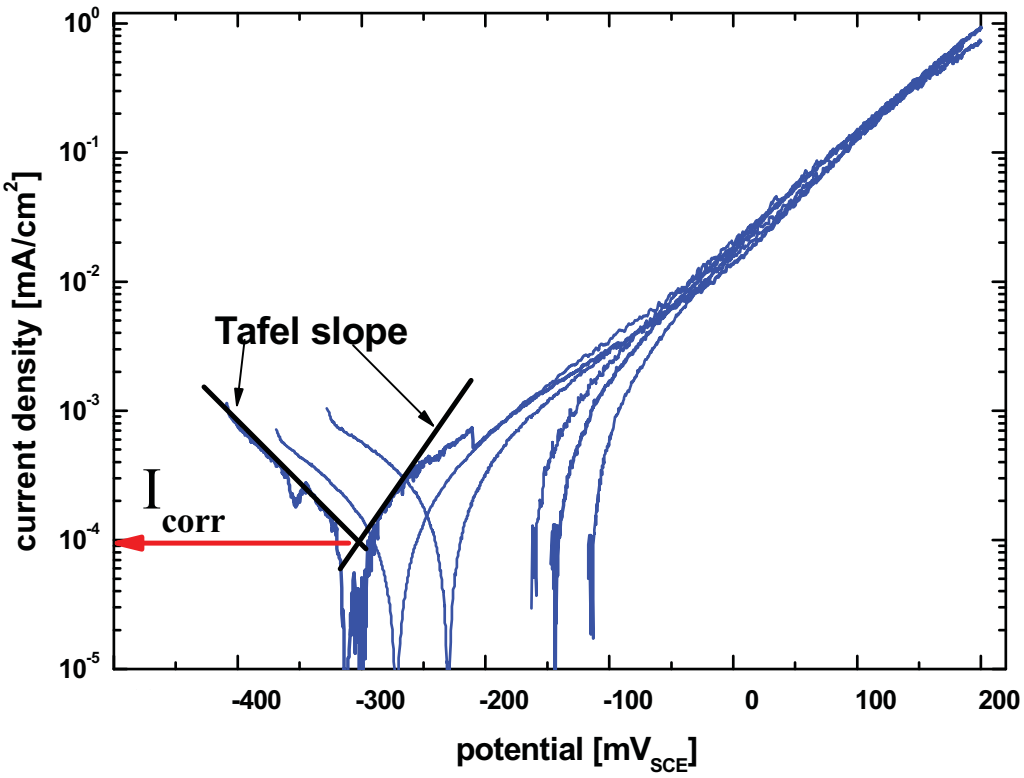

Figure 5.8: Potentiondynamic polarisation curves obtained for the system Mo-Cr, where three samples from the same deposition run have been measured. Determination of I_{corr} by Tafel slope extrapolation.

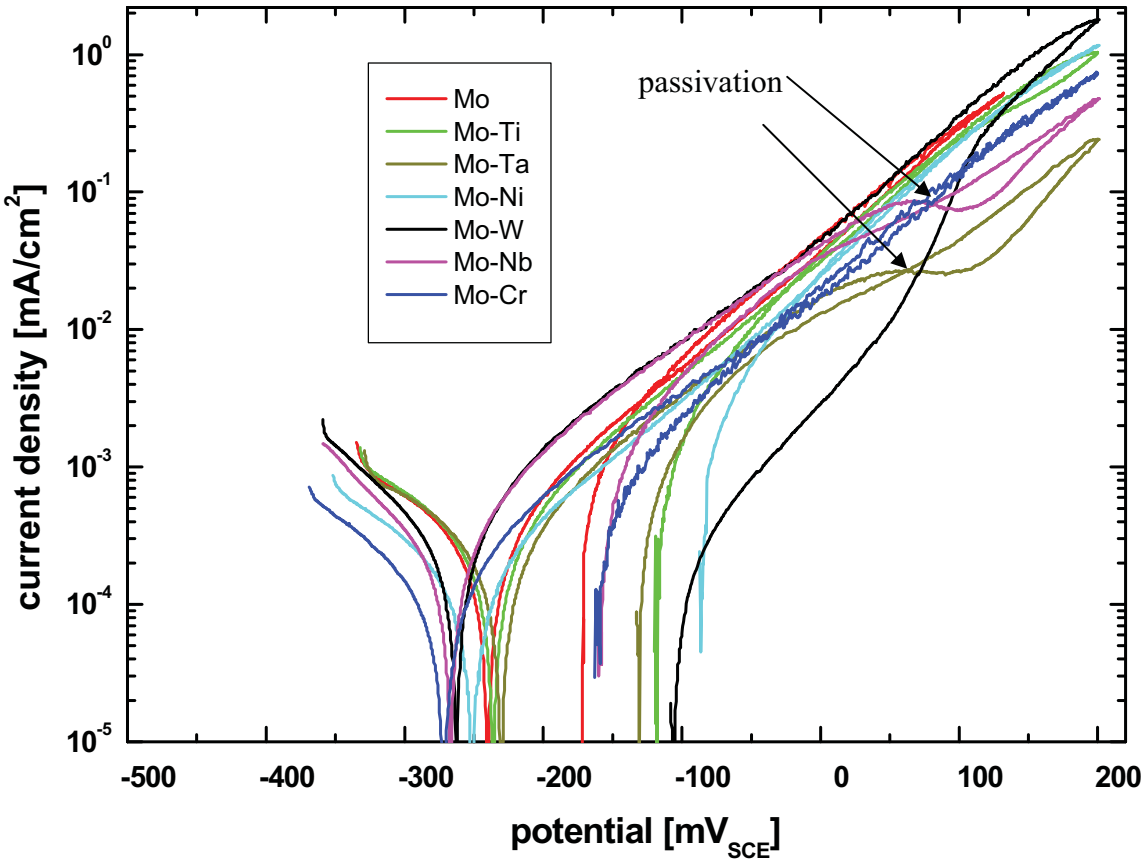

Figure 5.9: Potententiodynamic polarisation curves of Mo and binary Mo alloy thin film systems investigated. Mo-Ta and Mo-Nb thin film systems show passivation at relatively high potentials.

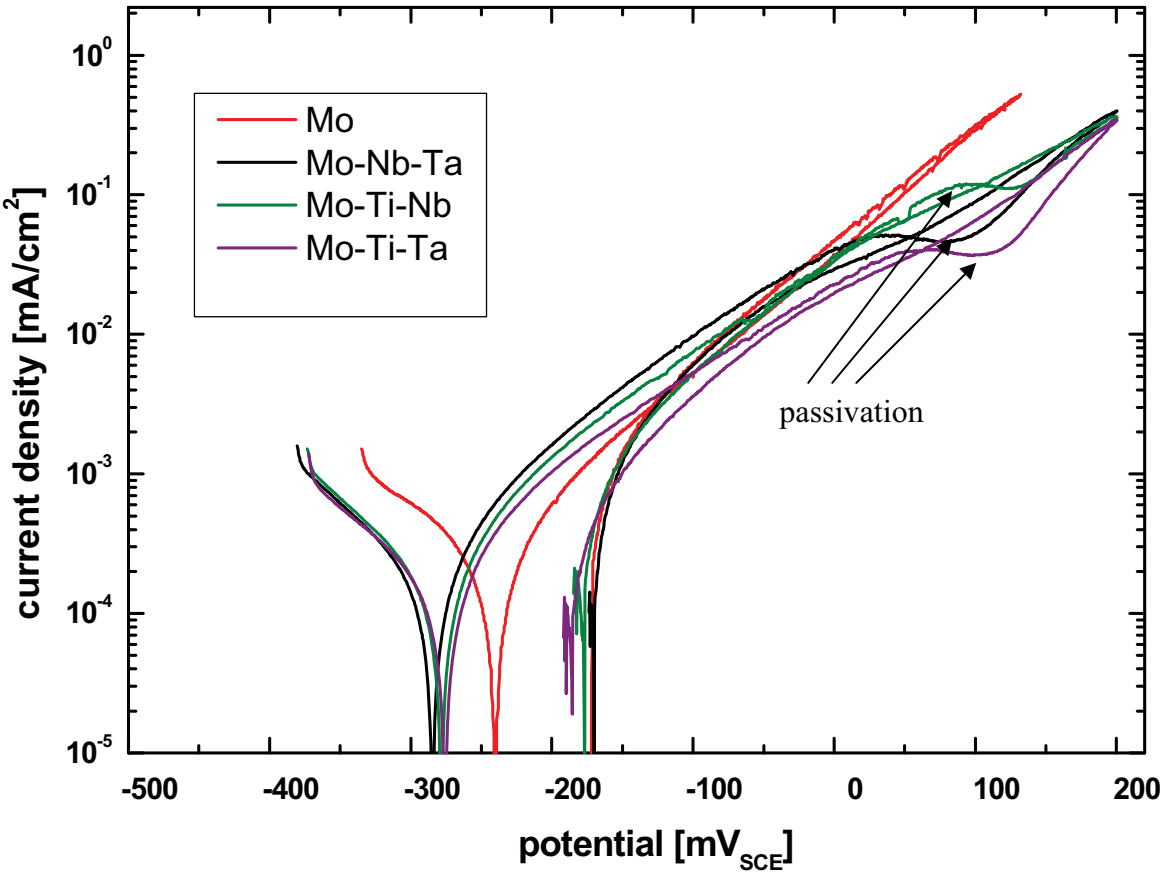

Figure 5.10: Potentiodynamic polarisation curves of Mo and ternary Mo alloy film system investigated. The ternary alloys show passivation at relatively high potentials.

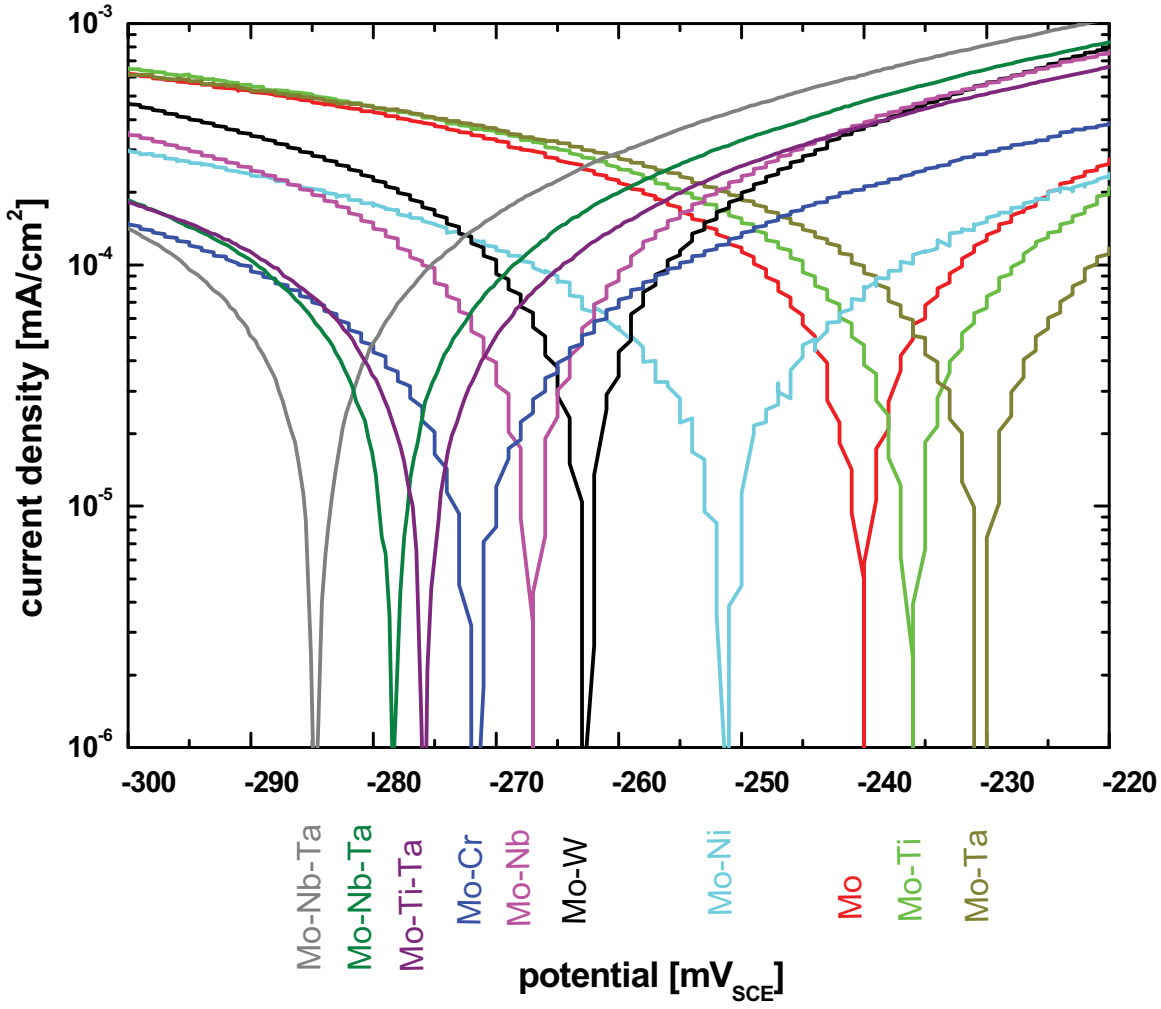

Figure 5.11: Potentiodynamic polarisation curves of the Mo alloy thin film systems investigated. All corrosion potentials lie within the scatter band of ± 40 mV.

5.6. Impedance Spectroscopy

To determine the polarisation resistance R_P, electrochemical impedance spectroscopy in a 0.9 % NaCl aqueous solution (room temperature, open circuit potential, ±10 mV, 1 mHz – 500 kHz) was performed. R_P was calculated from the Nyquist plots and found to increase with immersion time (see Fig. 5.12). It can thus be concluded that a layer with a better protection is generated by immersion time. This may be thru a thicker or denser oxide film.

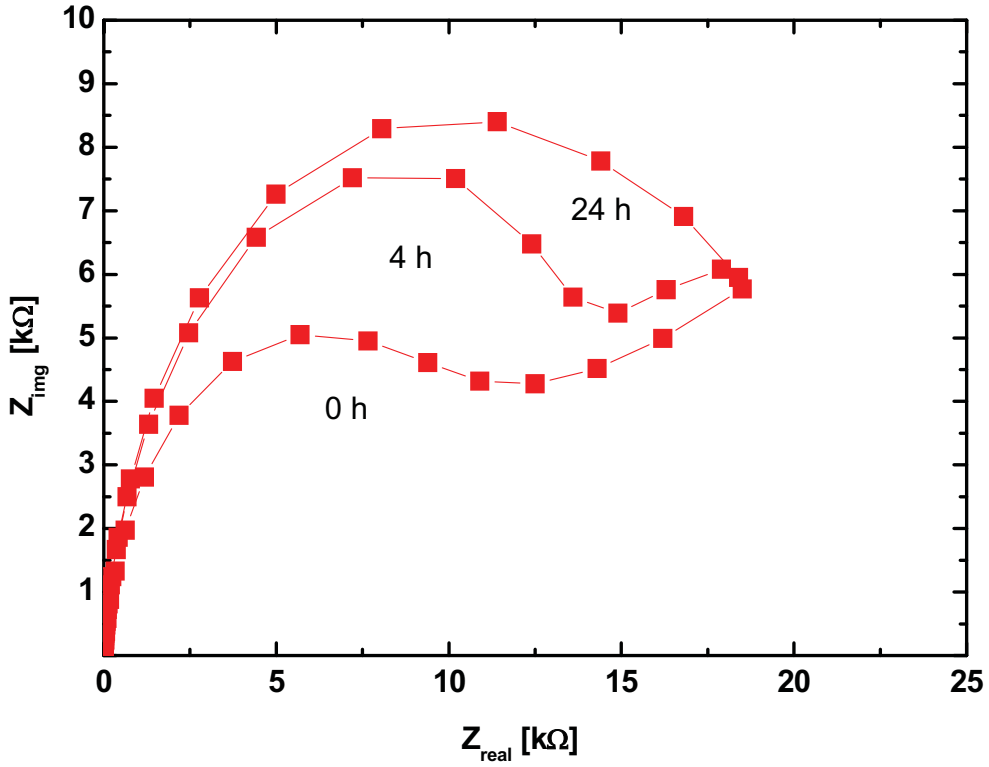

Figure 5.12 Nyquist-diagram of a Mo thin film in 0.9 % NaCl aqueous solution (room temperature) obtained directly after immersion and after 4 h and 24 h of exposure in the test solution.

To obtain information about data scattering, three samples from the Mo-W system have been measured. There an R_P value of 16 ± 1kΩ was obtained (see Fig. 5.13).

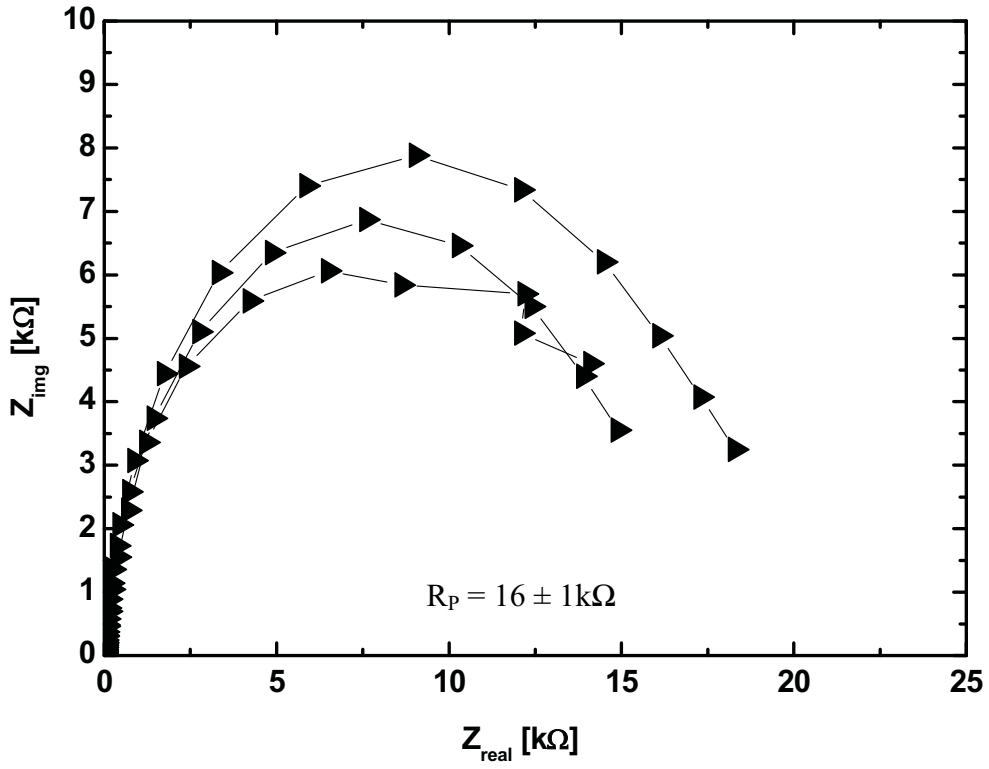

Figure 5.13: Nyquist-diagramm of Mo-W thin film in 0.9 NaCl aqueous solution (room temperature). Three samples of the same depositon run have been measured after 24h of exposure in the test solution

It can bee seen from Fig. 5.14, that alloying of Mo films with some smaller percentage of Ti, Ni, Nb, Ta and W only results in small changes of R_P. The lowest value (equal to the highest corrosion rate) was obtained for the Mo and Mo-W films. However, adding Cr results in a dramatic change of the Nyquist plot and an increase of the polarization resistance from values of about 20 to 116 kΩ (see Fig. 5.14 and Table 5.5). It has to be mentioned that only one species was available for this investigation. Results of Mo-Cr alloy says for a pronounced improvement of corrosion properties. All other tests did not confirm this to the same extent. Therefore result of Mo-Cr alloy is doubtful.

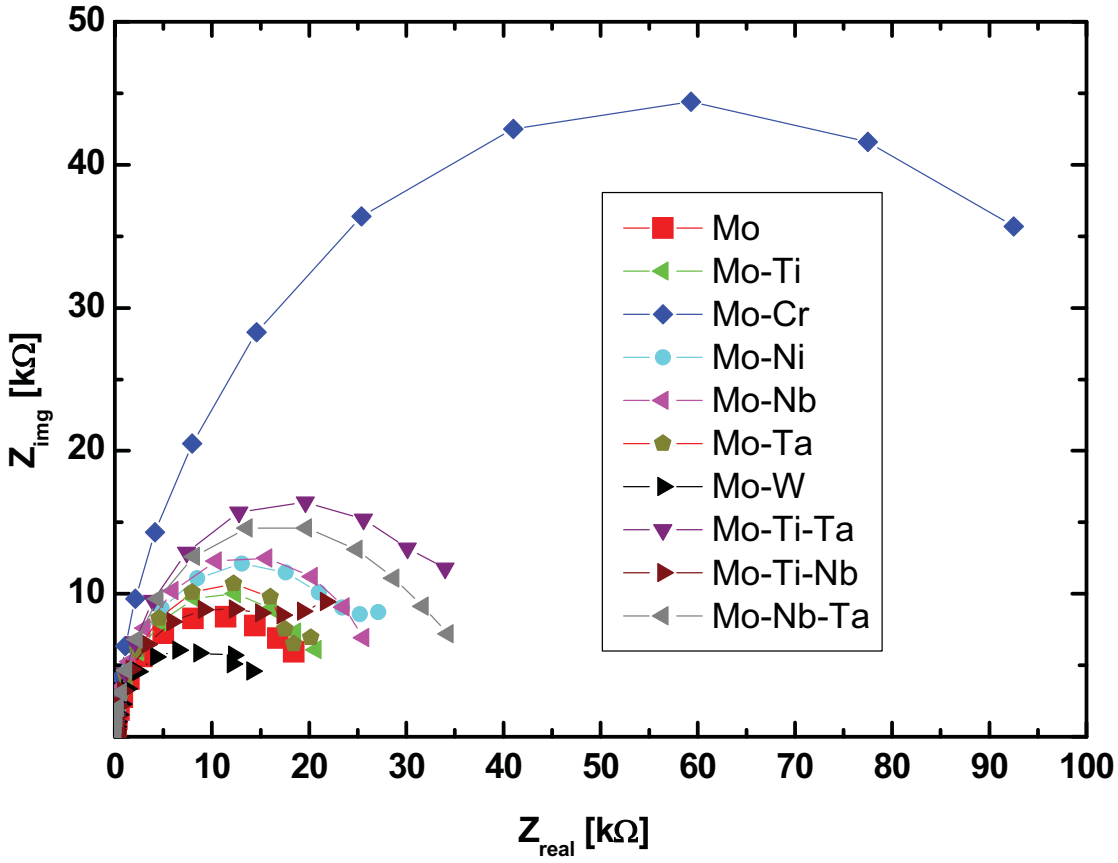

Figure 5.14: Nyquist-diagram of Mo alloy thin film systems obtainded in 0.9 % NaCl aqueous solution (room temperature) after 24 h of exposure in the test solution.

Table 5.5: Polarization resistance and ranking of the investigated Mo alloy thin film systems.

Alloy system	Polarization resistance [kΩ]	Ranking
Mo	20 ± 1	
Mo-Ti	24 ± 1	
Mo-Cr	116 ± 1	
Mo-Ni	28 ± 1	Mo-Cr
Mo-Nb	30 ± 1	Mo-Nb, ternary alloys
Mo-Ta	24 ± 1	Mo-Ni, Mo-Ta, Mo-Ti
Mo-W	16 ± 1	Mo, Mo-W
Mo-Ti-Ta	38 ± 1	
Mo-Ti-Nb	22 ± 1	
Mo-Nb-Ta	36 ± 1	

5.7. Exposure Tests

Exposure tests were done in a climatic test chamber at 85 % relative humidity and 85°C for 168 h. The mass gain loss was measured by weighing the sample before and after exposure to the corrosive environment. The measured mass changes are in the range of 10 to 420 µg (see Table 5.6). It has to be noted that the lower values are close to the resolution limit of the precision balance used. Nevertheless it can be seen from Table 5.6 that for the alloying systems Mo-Ti and Mo-Ta no specific mass gain was obtained, whereas for unalloyed Mo and for the alloying systems Mo-Ni and Mo-W the highest values have been observed. This corresponds also to the visual appearance of the film surfaces after exposure (see Fig. 5.15). For Mo, Mo-Ni and Mo-W intense blue colourations can be seen, while the other films show yellowish to brownish colours. The optical properties of molybdenum depend strongly on oxygen vacancy concentration [55]. However, the characterization and quantification of oxygen vacancies is rather difficult and beyond the scope of this thesis.

Table 5.6: Mass gain loss and ranking of investigated Mo alloy thin film systems.

Alloy system	Film thickness [nm]	Mass change [mg]	Specific mass change [mg/cm²]	Ranking
Mo	2300	0.42	0.016	
Mo	250	0.3	0.012	
Mo-Ti	220	-0.01	-0.00039	
Mo-Cr	2300	0.14	0.006	
Mo-Cr	250	0.06	0.0038	
Mo-Ni	220	0.27	0.01	Mo-Ti, Mo-Ta
Mo-Nb	2300	0.18	0.0084	Mo-Cr, Mo-Nb
Mo-Nb	220	0.15	0.0058	Mo-Ni, ternary alloys
Mo-Ta	220	-0.01	-0.00039	Mo-W, Mo
Mo-W	2300	0.33	0.014	
Mo-W	220	0.32	0.012	
Mo-Ti-Ta	170	0.23	0.009	
Mo-Ti-Ta	400	0.19	0.007	
Mo-Ti-Nb	400	0.23	0.009	
Mo-Nb-Ta	400	0.23	0.009	

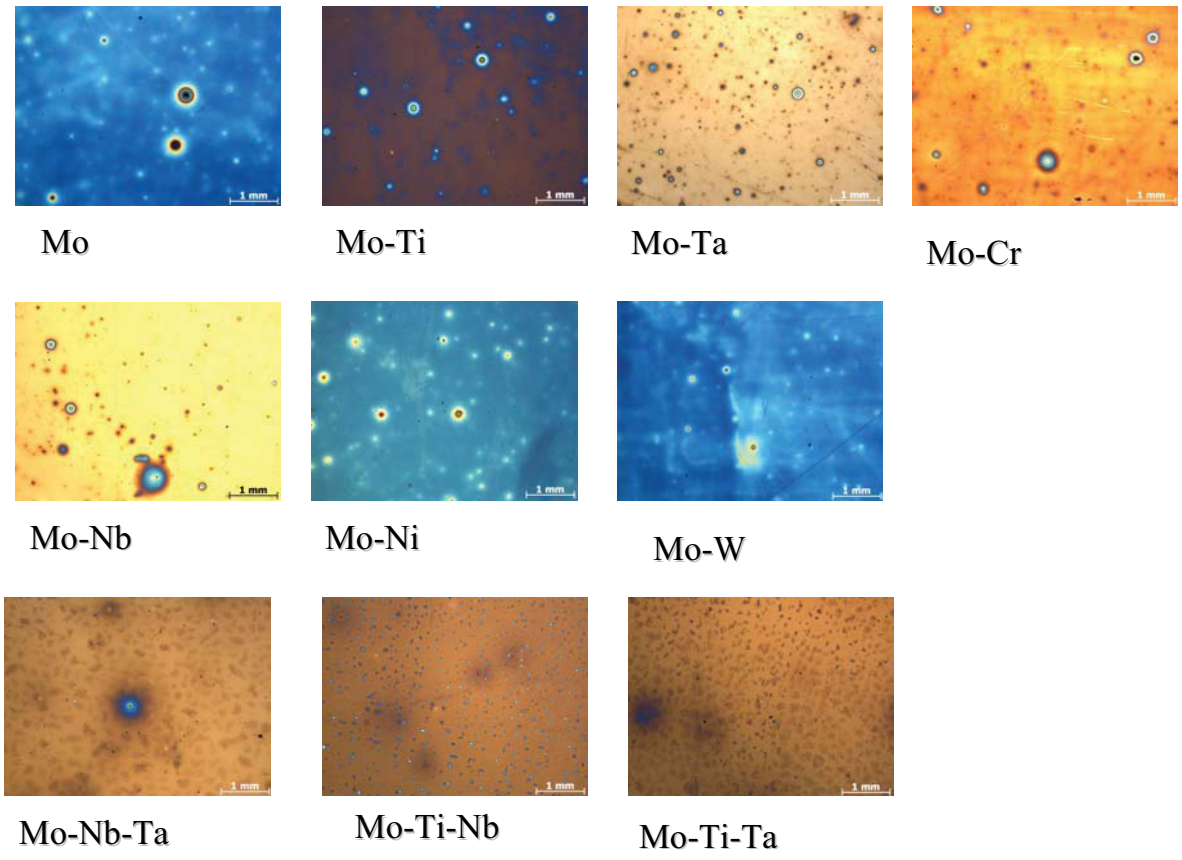

Figure 5.15: Light optical micrographs of Mo and Mo alloy thin films after exposure for 168 h in a climatic test chamber at 85 % relative humidity and 85°C.

The oxide films formed during the exposure were too thin to be detected in SEM cross-sections (see Fig. 5.16). To obtain more information about their nature, Raman spectroscopy investigations and XPS measurements had been done on the oxidized film surfaces (see following chapters).

a)

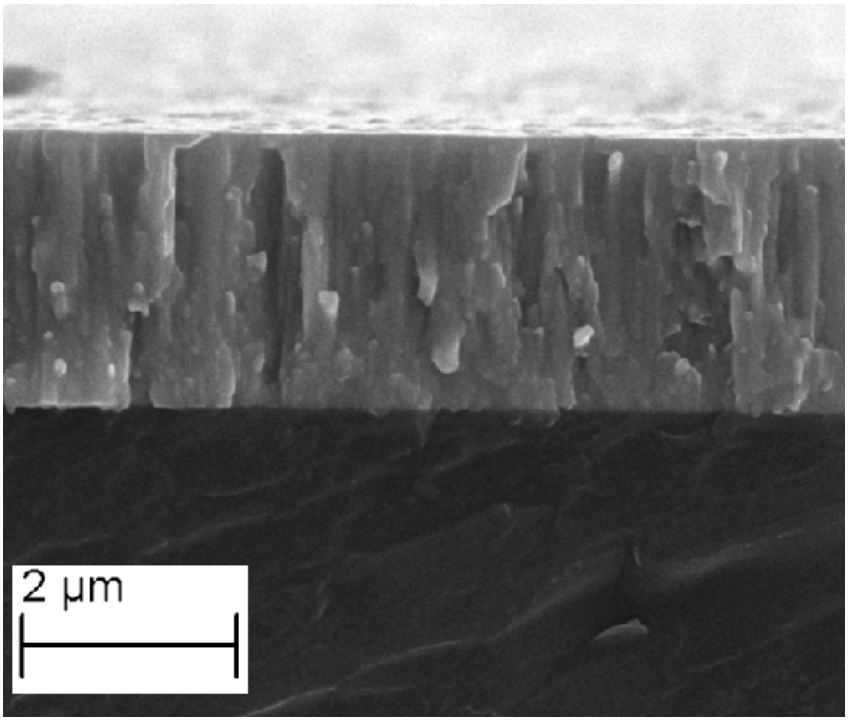

b)

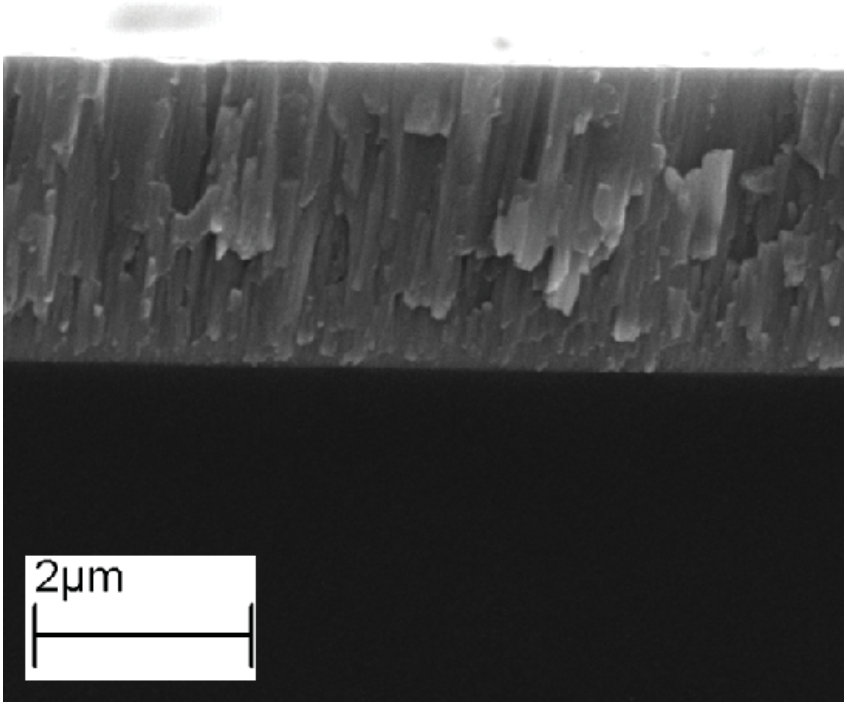

Figure 5.16: Cross-sectional fracture surfaces after exposure to the climatic test chamber at 85 % humidity and 85°C a) Mo, b) Mo-Cr.

5.8. Raman Spectroscopy

Raman spectroscopy was done on the oxidized film surfaces, after 168h of exposure to the climatic test chamber at 85 % humidity and 85 °C. Fig. 5.14 shows the Raman spectra of the investigated films as well as MoO_2 and MoO_3 powder for comparison. The surfaces of the oxidized films show peaks, which are less sharp and broader compared to the powder standards. This may result from the low thickness and high structural disorder of the oxide layers formed during low-temperature oxidation. Usually, metals are not Raman active, whereas oxides often show intense Raman bands [56]. This is in good agreement with the as-deposited Mo film surface, where no significant intensity of Raman peaks can be seen. Standard spectra are very limited and for the special investigated alloy systems in this thesis, just a few spectra have been found. The low intensity of the spectrum of the Mo-Ta film indicates a very thin oxide film and correlates well with the low mass gain after exposure (see Table 5.6). Furthermore, the oxidized films are indicative for formation of MoO_2 and MoO_3 [55, 57], as confirmed by the Raman spectra of MoO_2 and MoO_3 powders shown in Fig. 5.14. Moreover, it can be seen in Fig 5.14, that there are no significant differences of the peak positions for the unalloyed film and for alloying with Ti, Ni, Nb and W. However the Mo-Cr film shows – in addition to the peaks originating of MoO_2 and MoO_3 – a pronounced Raman peak at ~ 880 cm^{-1}, which is related to the formation of chromium oxides [58, 59]. It can thus be concluded that these chromium oxides show a passivating nature, explaining the excellent performance of Mo-Cr films in the corrosion test.

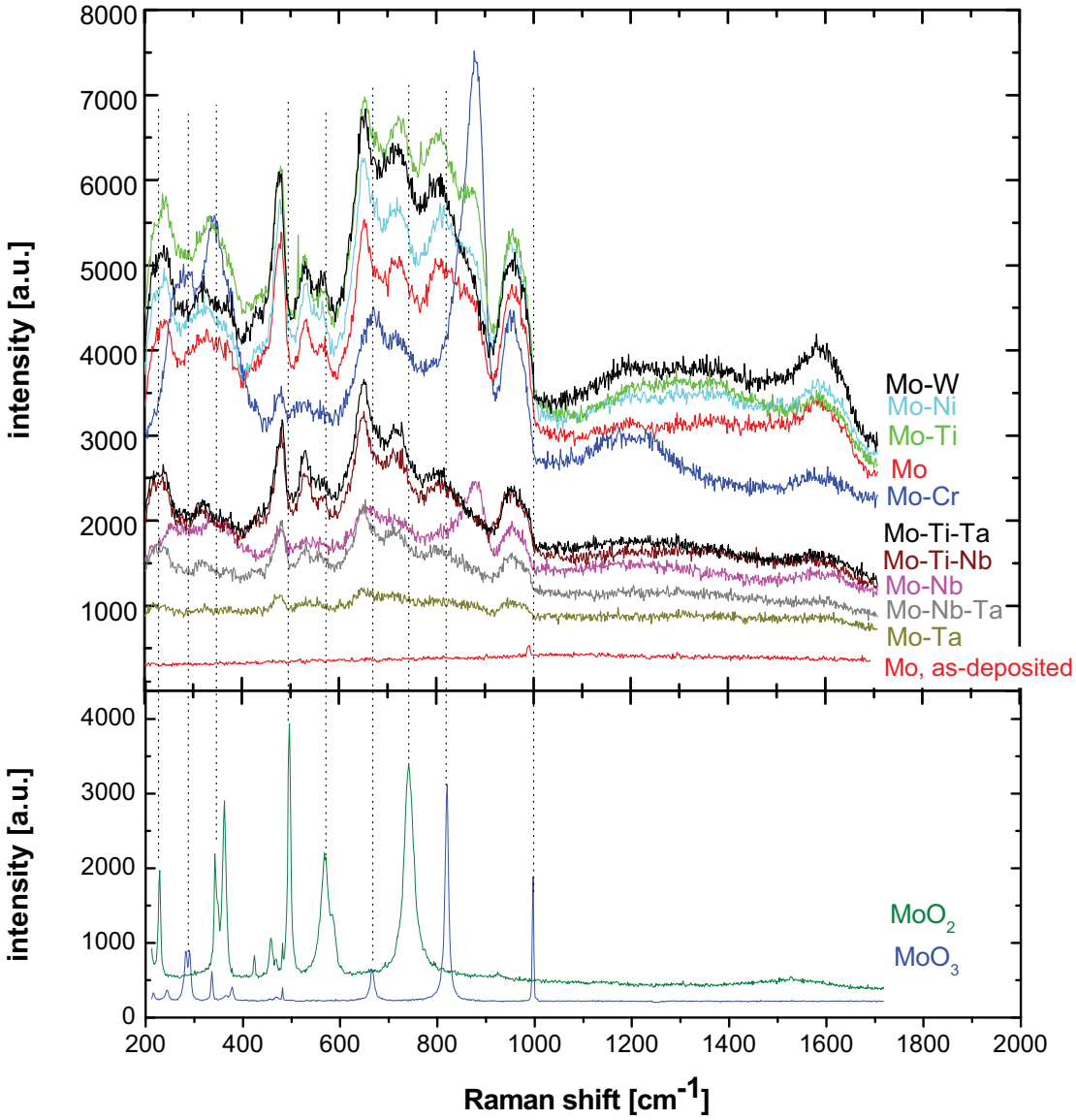

Figure 5.17: Raman spectra of the as-deposited Mo film and the Mo alloy systems oxidized for 168 h at 85°C and 85 % relative humidity. The Raman spectra of MoO_2 and MoO_3 powder are given for comparison.

5.9. X-Ray Photoelectron Spectroscopy

To obtain more information about the nature of the oxide films, XPS analysis was performed on the oxidized film surfaces of Mo and binary Mo alloys exposed to 85 % humidity and 85 °C for 168 h and as reference for as-deposited Mo and Mo-Cr films. The samples had been measured directly on the surface and after sputtering to a depth of ~50 nm. Typical examples of these measurements are presented in Figs. 5.15 to 5.17. The spectrum itself contains a series of lines that arise from the unique excitation energies of each present element. Generally, all elements except H are detectable while the spectra features vary. Elements like N and O with 1s orbital energies reveal single lines, whereas spin-orbit splitting causes two separate lines for p, d and f orbitals [60]. The spectra obtained for the surface (see Fig. 5.18) of oxidized Mo and Mo alloys exhibit peaks of carbon, nitrogen, oxygen and molybdenum and in 50 nm depth (see Fig. 5.19) in addition the respective alloying element (except Ti) was seen. The reason that no Ti peak was found is presently unclear.

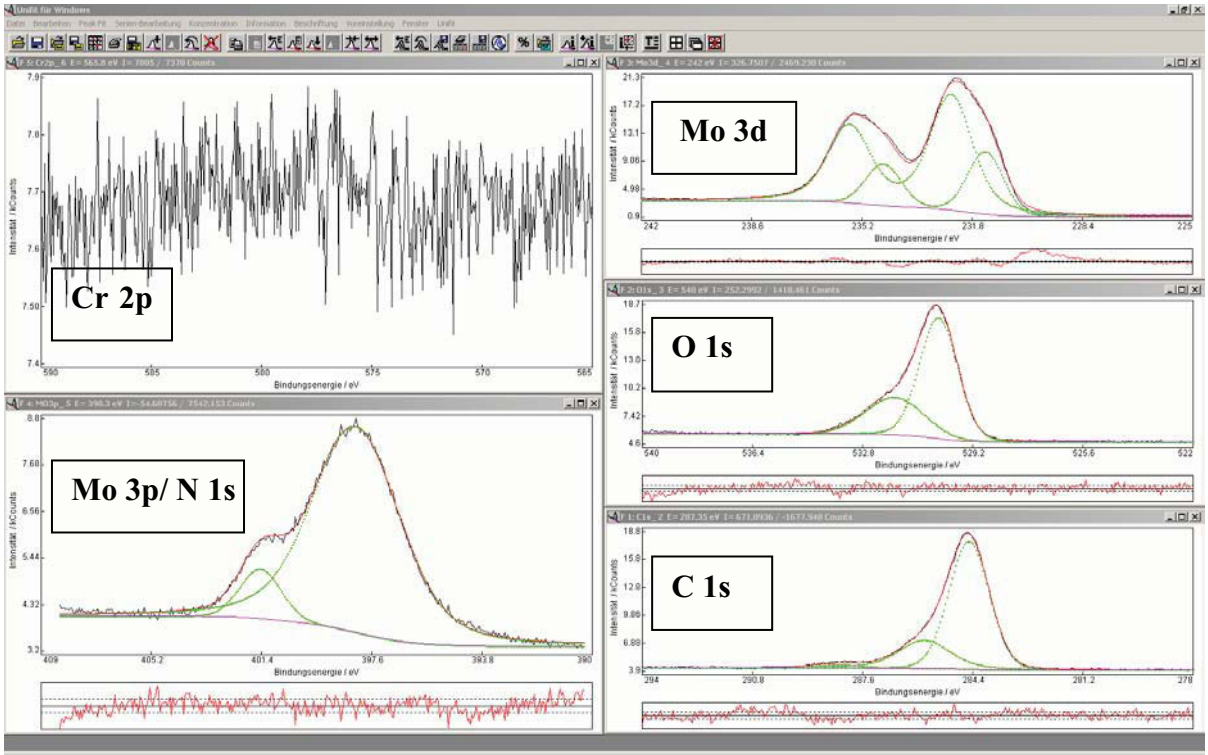

Figure 5.18: Screenshot of XPS spectra of Mo-Cr oxidized film of the surface, after exposing to 85 % humidity and 85 °C for 168 h. XPS core level spectra with fitted subpeaks of Cr, Mo 3d, Mo 3p/N, O and C are shown.

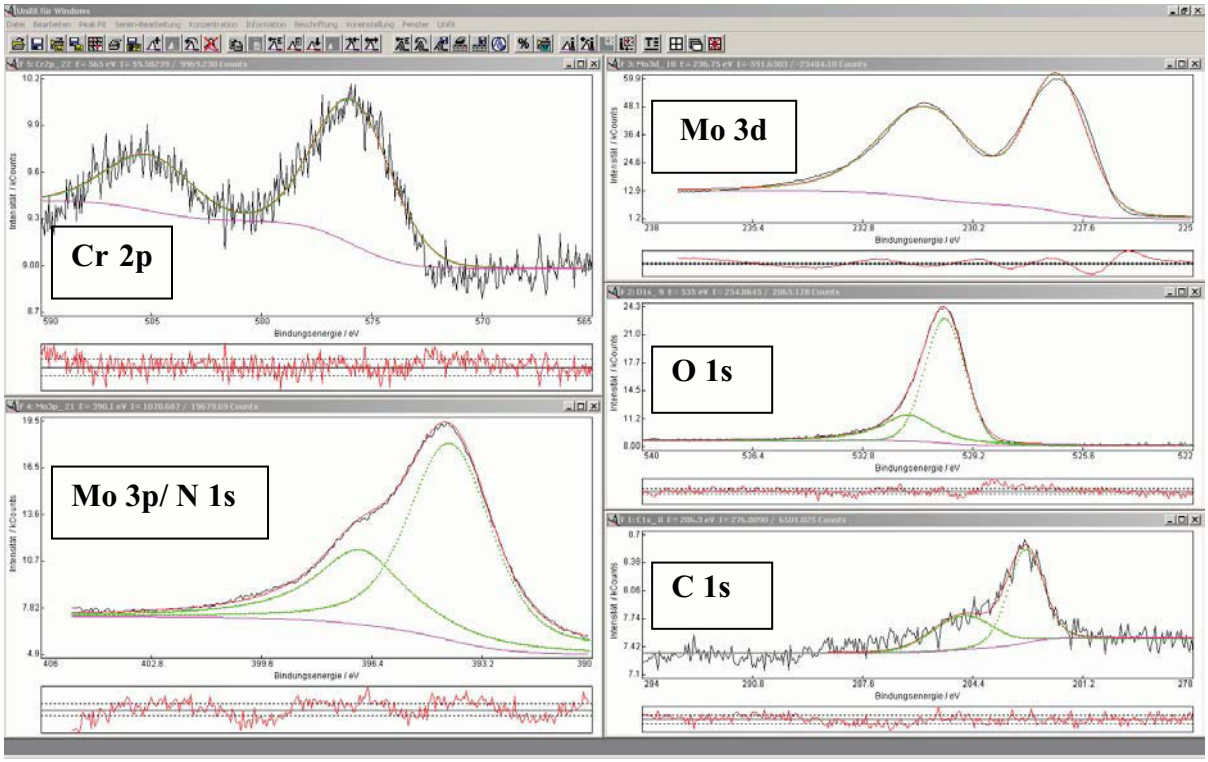

Figure 5.19: : Screenshot of XPS spectra of Mo-Cr oxidized film after sputtering to a depth of ~ 50 nm, exposed to 85 % humidity at 85 °C for 168 h. XPS core level spectra with fitted subpeaks of Cr, Mo 3d, Mo 3p/N, O, C and Cr are shown.

Commonly, peak shifts are caused by different oxidation states, different chemical environments, different lattice sites, etc [60]. Fig. 5.20 defines on the surface a mixture of two different oxidation states of Mo (Mo^{4+} and Mo^{6+}) exemplarily for the oxidized Mo-Cr film. This was obtained most of the investigated films, unless for the samples alloyed by Nb and Ta where only one contribution (Mo^{4+}) could be detected on the surface. This correlates well with the low intensity of the Raman peaks of Mo-Ta and Mo-Nb (see Fig. 5.17), indicating a thin oxide film with a low disorder. After sputtering to a depth of ~50 nm, lower bond energy and higher intensity for the Mo peak, corresponding to the metallic Mo, is seen for all coatings.

a)

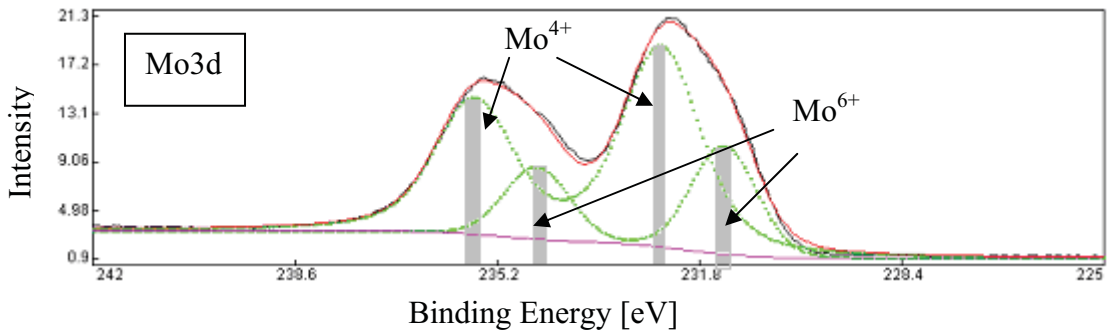

b)

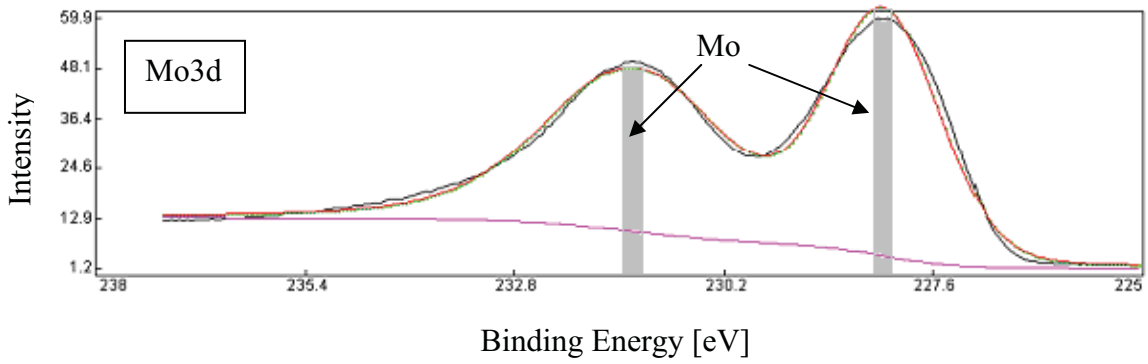

Figure 5.19: XPS core level spectra with fitted subpeaks of 3d Mo doublets of Mo-Cr oxidized films. a) On the surface two contributions were detected. b) In 50 nm deep one contribution with lower binding energy and higher intensity was detected. Relative binding energy ranges are given according Refs. [39, 61, 62]

In Table 5.7 a summary of the relative composition determined by XPS of the as-deposited is shown. The spectra exhibit peaks of carbon and oxygen in addition to molybdenum and for the Mo-Cr film the alloying element Cr. For the Mo-Cr film lower Mo and higher O values are obtained. This may result from a more stable oxide film and correlates well with the excellent performance of Mo-Cr in the corrosion series.

Table 5.7: Summary of the relative content of Mo, O, C, N and Cr of as-deposited Mo and Mo-Cr films. The samples had been measured directly on the surface (a) and at a depth of ~50 nm (b).

a) surface						**b) 50 nm**				
Alloy system	**Mo** [at %]	**O** [at %]	**C** [at %]	**N** [at %]	**Cr** [at %]	**Mo** [at %]	**O** [at %]	**C** [at %]	**N** [at %]	**Cr** [at %]
Mo	35	30	35	0	0	100	0	0	0	0
Mo-Cr	21	55	33	0	1.3	79	18	0	0	2.8

The spectra obtained from the surface of oxidized Mo and Mo alloys (see Table 5.8) exhibited peaks of carbon, nitrogen, oxygen, molybdenum and additionally in 50 nm depth the respective alloying element (except Ti). For the spectra of the oxidized films no significant differences in the measurement on the surface for the unalloyed and alloyed films were detected. The alloying elements are not seen on the surface, this may be a result of their preferential chemical dissolution.

In ~50 nm depth, for the oxidized film systems Mo-Ta and Mo-Nb the lowest O, C and N values and for Mo the highest ones were obtained. This correlates well with the low intensity of the Raman peaks of Mo-Ta and Mo-Nb (see Fig. 5.17), indicating a thin oxide film with a low disorder. Moreover, in 50 nm depth for the unalloyed oxidized film and for alloying with Ti, Cr, Ni and W an increase of N and O can be seen. This may be explained by the C content which generally decreases very strongly and thus the relative proportions of the other components increase. Even an absolute decline of the content can result in a relative increase. Moreover, it has to be mentioned that the Mo and N peaks overlap in XPS, giving a high uncertainty in determining the N content. An absolute increase of O and N in deeper layers seems to be highly unlikely. Further it has to be mentioned that the element H is not detectable by XPS measurements and no information about expected hydroxides can be achieved.

Table 5.8: Summary of the relative content of Mo, O, C, N and the respective alloy element of the Mo and Mo alloy oxidized thin film systems exposed for 168h to 85 % relative humidity and 85 °C investigated by XPS. The samples had been measured directly on the surface (a) and at a depth of ~50 nm (b).

	a) surface					**b) 50 nm**				
Alloy system	**Mo** [at %]	**O** [at %]	**C** [at %]	**N** [at %]	**alloying element** [at %]	**Mo** [at %]	**O** [at %]	**C** [at %]	**N** [at %]	**alloying element** [at %]
Mo	12	30	54	3	0	32	33	9	24	0
Mo-Ti	10	29	58	2.7	0	34	33	10	22	0
Mo-Cr	11	29	57	3	0	33	34	8	22	1.6
Mo-Ni	10	28	58	3.8	0.05	35	36	9	19	0.09
Mo-Nb	12	32	53	3	0	83	13	2.6	0	1.5
Mo-Ta	10	30	57	3.3	0	81	12	5	0	1.9
Mo-W	10	30	55	2.8	0	30	32	6	30	1.4

6. Summary and Conclusions

The aim of this work was to evaluate the effect of low contents of the alloying elements Ti, Cr, Ni, Nb, Ta or W, respectively, in sputter deposited Mo films on their oxidation and corrosion resistance. The first step was the formation of these alloys on glass substrates by magnetron sputtering from mosaic targets. The film thickness was characterized using SEM on fractured cross-sections and 3D optical profilometry on the steps of partly masked and thus uncoated substrate areas. XRD and EDX analyses were conducted to investigate structure and coating composition. Electrical, oxidation and corrosion properties have been determined by a four-point method, by exposure in a climatic test chamber and by potentiodynamic polarization experiments and electrochemical impedance spectroscopy in 0.9 % NaCl aqueous solution. To get more information about the nature of the oxide film, Raman spectroscopy and XPS investigations have been done on the oxidized film surfaces, formed during exposure in the climatic test chamber.

Single phase Mo-based solid solutions were successfully prepared and the content of the alloying elements was in the range between 3.2 and 5.2 at.-%. The electrical resistivity of unalloyed Mo film agrees well with literature data and was only slightly increased by the alloying elements; except the addition of Ni results in a three times higher value. In the corrosion and oxidation behaviour, relatively small differences have been observed. Nevertheless, some general tendencies can be pointed out from the combination of tests performed. The results obtained from the corrosion tests are summarised in Table 6.1.

Table 6.1: Summary of results of corrosion tests. Mo and Mo-alloys are listed from best to worst performance.

Potentiodynamic polarization (1h)	Impedance spectroscopy (24h)	Exposure test (168h)	Ranking
Mo-Cr	Mo-Cr	Mo-Ta	
Mo-Ni	Mo-Nb	Mo-Ti	
Mo-Nb	ternary alloys	Mo-Cr	Mo-Cr
ternary alloys	Mo-Ni	Mo-Nb	Mo-Nb, Mo-Ta, Mo-Ti
Mo-Ti	Mo-Ta	Mo-Ni	ternary alloys, Mo-Ni
Mo-Ta	Mo-Ti	ternary alloys	Mo-W, Mo
Mo-W	Mo	Mo-W	
Mo	Mo-W	Mo	

Alloying with Cr shows the best performance in electrochemical impedance spectroscopy as well as in electrochemical polarization experiments and the Mo-Cr sample is within the top three ones in the exposure test in the climatic test chamber. These excellent corrosion properties of Mo-Cr are related to the change of oxide film structure from pure Mo oxide towards a Cr-enriched oxide film. These oxide films were too thin to be detected by XRD and in SEM cross-sections. In order to get more information about their nature, Raman spectroscopy and XPS investigation have been done on the oxidized film surfaces, formed during exposure in the climatic test chamber as well on as-deposited unalloyed Mo and Mo-Cr films.

The positions of the Raman peaks do not show significant differences for the unalloyed films and for alloying with Ti, Ni, Nb and W. The Mo-Cr film shows – in addition to the peaks originating from MoO_2 and MoO_3 – a pronounced Raman peak at ~ 880 cm^{-1}, which is related to the formation of chromium oxides. It can thus be concluded that these chromium oxides show a passivating nature, explaining the excellent performance of Mo-Cr films. Within the investigations of as-deposited samples for the Mo-Cr film lower Mo and higher O concentrations by XPS have been obtained compared to the unalloyed Mo-film. This might be connected to a more stable oxide film in the Mo-Cr system. For the oxidized film surfaces, no significant differences of the relative composition for the unalloyed and alloyed films could be detected. After sputtering to a depth of 50 nm for the oxidized film systems Mo-Ta and Mo-Nb, the lowest O, C and N values were obtained. This correlates well with the low intensity of the Raman peaks of Mo-Ta and Mo-Nb indicating a thin oxide film with a low disorder.

Finally, it can be concluded that the effect of low contents of alloying elements on the corrosion and oxidation behaviour of Mo films is relatively small. Nevertheless, some general tendencies can be pointed out from the combination of tests performed. Alloying with Cr shows the best performance resulting in the lowest corrosion density in electrochemical polarization experiments, the highest polarization resistance in electrochemical impedance spectroscopy and the Mo-Cr sample is within the top three ones in the exposure test in the climatic test chamber. While alloying by Ti, Ni, Nb and Ta yields corrosion and oxidation properties better than the unalloyed Mo films, alloying by W does not show a benefical effect. This is most probably due the similar chemical behaviour and oxide structure of Mo and W.

7. References

[1] Y. Kuo, Thin Film Transistors, Materials and Processes, Kluewer Academic Publishers, 322- 324, 2004.

[2] http://www.rembar.com/moly.htm, (01.04.2009).

[3] W. d. Boer, Active Matrix Liquid Crystal Displays, Elsevier Science Publishers, Amsterdam, 29-30, 2005.

[4] Y. W. Ko, D. H. Choi, Journal of Korean Physical Society, 33, 415-418, 1998.

[5] V.S. Sastri, Corrosion Inhibitors Principles and Applications, John Wiley & Sons Ltd, Chichester, 1998.

[6] N. Birks, G.H. Meier and F.S. Pettit, Introduction of the High-Temperature Oxidation of Metals, 2nd Ed, Cambridge University Press, Cambridge, 2006.

[7] R. Bürgel, Handbuch Hochtemperatur-Werkstofftechnik, Friedr. Vieweg & Sohn Verlagsgesellschaft, Braunschweig/Wiesbaden, 2001.

[8] L. Hultman, J.E. Sundgren, in R.F. Bunshah, S.M. Rossnagel, G.E. McGuire (eds.), Handbook of Hard Coatings, Deposition Technologies, Properties and Applications, Noyes Publikations, New Jersey, 2001.

[9] R.A. Häfer, Oberflächen- und Dünnschicht- Technologie, Teil I: Beschichtungen von Oberflächen, Springer-Verlag, Berlin, Heidelberg, 1987.

[10] G. Kienel, K. Röll (eds.), Vakuumbeschichtung 2, Verfahren und Anlagen, VDI Verlag, Düsseldorf, 1995.

[11] P.H. Mayrhofer, Materials Science Aspects of Nanocrystalline PVD Hard Coatings, PhD-Thesis, University of Leoben, 2001.

[12] D.M. Mattox, Handbook of Physical Vapor Deposition (PVD) Processing, Noyes Publications, New Jersey, 1998.

[13] J. Edwards, Coating and Surface Treatment Systems for Metals, Finishing publications, Hertfordshire, 1997.

[14] A. Laarmann, T. Wenz, Modern Surface Technology, WILEY-VCH, Weinheim, 2006.

[15] A. Grill, Cold Plasma in Materials Fabrication, IEEE Press, New York, 1994.

[16] N.B. Chapman, Glow Discharge Processes, John Wiley, New York, 1984.

[17] B. Rother, J. Vetter, Plasma-Beschichtungsverfahren und Hartstoffschichten, Dt. Verlag für Grundstoffindustrie, Leipzig, 1992.

[18] P.H. Mayrhofer, Materials Science Aspects of Nanocrystalline PVD Hard Coatings, PhD-Thesis, University of Leoben, 2001.

[19] I. Petrov, F. Adibi, J.E. Greene, W. D. Sproul, W.-D. Münz, J. Vac. Sci. Technol. A 10 (5) (1992) 3283.

[20] J.E. Greene, Handbook of Crystal Growth, Elsevier Science Publishers, Amsterdam, 1993.

[21] H. A. Jehn, in Advanced Techniques for Surface Engineering, W. Gissler, H. A. Jehn (eds.), Kluwer Academic Publishers, Dordrecht, 1992.

[22] J.A. Venables, G. D. T. Spiller, M. Hanbücken, Rep. Prog. Phys. 47 (1984) 399.

[23] M. Ohring, Materials Science of Thin Films, Academic Press, San Diego, 2nd edition, 2002.

[24] B.A. Movchan, A. V. Demchishin, Phys. Met. Metallogr. 28 (4) (1969) 83.

[25] J. A. Thornton, J. Vac. Sci. Technol., 11 (4) 666-670, 1974.

[26] J.A. Thornton, J. Vac. Sci. Technol., 12 (4) 830-835, 1975.

[27] P. B. Barna and M. Adamik, in Y. Pauleau, P. B. Barna (Eds.), Protective Coatings and Thin Films, Synthesis, Characterization and Applications, Kluwer Academic Publishers, Dordrecht, 1997.

[28] I. Petrov, P. B. Barna, L. Hultman and J. E. Greene, Microstructual evolution during film growth. J. Vac. Sci. Technol. A, 21(5) 117-128, 2003.

[29] R. Messier, A.P. Giri, R. A. Roy, J. Vac. Sci. Tech. A 2 (2) 500-503, 1984.

[30] J. A. Thornton, Ann. Rev. Mater. Sci. 7 (1977) 239-260.

[31] G. Mori, Korrosionskunde Skript, Montanuniversität Leoben, SS 2006/2007.

[32] J.R. Davis, Corrosion, Understanding the Basics, ASM International, Ohio, 2000.

[33] J. H. Seo, B. H. Seo, S. H Lee, I. K Lee, J. H. Jeon, H. Choe, K. W Lee, Digest of Technical Papers – SID International Syphosium, 38 (1), 381-384, 2007.

[34] S. Müller, E Scharf, G. Umlauff, W. Sutor, Grundlagen metallischer Werkstoffe Korrosion und Korrosionsschutz, VEB Deutscher Verlag für Grundstoffindustrie, Leipzig, 95, 1988.

[35] G. Mori, Corrosion Testing script, University of Leoben, WS 2008/2009.

[36] E. Kunze, Korrosion und Korrosionsschutz, Band 2: Korrosion der verschiedenen Werkstoffe, Wiley-VCH Verlag GmbH, Weinheim, 1133 -1134, 2001.

[37] M. Pourbaix, Atlas of Electrochemical Equilibria in Aqueous Solutions, NACE, Cebelcor, 272-279, 1974.

[38] http://www.webelements.com/molybdenum, (03.04.2009).

[39] K. Hashimoto, J. Bhattarai, X. Y. Li, P. Y. Park, J. H. Kim, E. Akiyama, H. Habazaki, A. Kawashima, K. Asami and K. Shimanura, The Electrochemical Society, 97-26, 369-383, 1998.

[40] P.Y. Park, E. Akiyama, H. Habazaki, A. Kawashima, K. Asami and K. Hashimoto, Corrosion Science, Vol 38, 1649-1662, 1996.

[41] E. McCafferty, Journal of the Electrochemical Society, 150 (5) B 238-B 247, 2003.

[42] Veeco metrology group, Wyko surface profilers, technical reference manual, Sept., 1999.

[43] W. Demtröder, Experimentalphysik 3, Atome, Moleküle und Festkörper, Springer, Berlin, 1996.

[44] B.D. Cullity, Elements of X-ray diffraction 2nd Ed., Edison-Wesley Publishing Company, Reading, 1978.

[45] E. Lifshin, X-ray Characerisation of Materials, WLEY-VCH, Weinheim, 1999.

[46] MDC, Four-point Probe Manual, Materials Development Corp., Geneva.

[47] H. Kuchling, Taschenbuch der Physik, Carl Hanser München, 2001.

[48] H. Willmann, PhD Thesis, Al-Cr-N thin film design for high temperature applications, University of Leoben, 2007.

[49] D.J. O`Connor, B.A. Sexton; R. St. C. Smart, Surface Analysis Methods in Materials Science, Springer, Berlin, 2003.

[50] Chair of Mineralogy and Petrology, at the University of Leoben, Austria, http://institute.unileoben.ac.at/mineralogy/Geraete.html#Analytical_Instruments.

[51] http://www.srim.org Version 2008.5.

[52] J.P. Biersack, L. Haggmark, Nucl. Instr. And Meth. 174, 257, 1980.

[53] J.F. Ziegler, J.P. Biersack, U. Littmark, The Stopping and Range of Ions in Matter, Pergamon Press, New York, 1996.

[54] F. Martin, P. Muralt and M.-A. Dubois, J. Vac. Sci. Technol. A 24, 946-952, 2006.

[55] F. Klabunde, M. Löhmann, J. Blasinq and T. Drüsedau, J. Appl. Phys. 80, 6266-6273, 1966.

[56] M. Dieterle, G. Weinberg and G. Mestl, Phys. Chem. Chem. Phys. 4, 812-821, 2002.

[57] W.H. Weber, Raman Scattering in Materials Science, Springer, Berlin, 2000.

[58] M. Dieterle and G. Mestl, Phys. Chem. Chem. Phys. 4, 822-826, 2002.

[59] D. Stanoi, G. Socol, C. Grigorescu, F. Guinneton, O. Monnereau, L. Tortet, T. Zhangd and I.N. Mihailescu, Mater. Sci. Engin. B. 118, 74-78, 2005.

[60] B. M. Weckhuysen and I. E. Wachs, J. Phys. Chem. B 101, 2793-2796, 1997.

[61] R. Franz, PhD Thesis, AlCrVN – Design of high-temperature low-friction coatings, University of Leoben, 2007.

[62] La Surface database, http://www.lasurface.com/accueil/index.php.

[63] NIST database, http://srdata.nist.gov/xps/.